Source parameter inversion for wave energy focusing to a target inclusion embedded in a three-dimensional heterogeneous halfspace

Pranav M. Karve[1], Arash Fathi[2], Babak Poursartip[1] and Loukas F. Kallivokas[1,2,*,†]

[1]*Department of Civil, Architectural and Environmental Engineering, The University of Texas at Austin, Austin, TX 78712, U.S.A.*
[2]*The Institute for Computational Engineering and Sciences (ICES), The University of Texas at Austin, Austin, TX 78712, U.S.A.*

SUMMARY

We discuss a methodology for computing the optimal spatio-temporal characteristics of surface wave sources necessary for delivering wave energy to a targeted subsurface formation. The wave stimulation is applied to the target formation to enhance the mobility of particles trapped in its pore space. We formulate the associated wave propagation problem for three-dimensional, heterogeneous, semi-infinite, elastic media. We use hybrid perfectly matched layers at the truncation boundaries of the computational domain to mimic the semi-infiniteness of the physical domain of interest. To recover the source parameters, we define an inverse source problem using the mathematical framework of constrained optimization and resolve it by employing a reduced-space approach. We report the results of our numerical experiments attesting to the methodology's ability to specify the spatio-temporal description of sources that maximize wave energy delivery. Copyright © 2016 John Wiley & Sons, Ltd.

1. INTRODUCTION

Cost-effective and reliable methods for the removal of crude oil or contaminant particles from the pores of geological formations play a crucial role in petroleum engineering, hydro-geology, and environmental engineering. To date, various extraction techniques that involve injecting water, solvents, polymers, or steam into the geo-formation of interest have been used for this purpose. In the field of petroleum engineering, these methods are classified into two categories: (a) the conventional oil recovery methods (water/gas flooding) and (b) the enhanced oil recovery (EOR) methods (chemical/steam injection). Typically, the EOR methods are employed after about 50–60% of the original oil in place has been produced using the conventional oil recovery methods. In general, the EOR methods are successful in extracting a part of the remaining crude oil [1]. However, the chemical-injection-based EOR methods suffer from sweep efficiency problems in low permeability areas, and the thermal EOR (steam injection) faces problems because of heat loss. Thus, efficient and economically competitive methodologies for extracting trapped particles from the pores of geo-formations remain desirable.

---

*Correspondence to: L. F. Kallivokas, Department of Civil, Architectural and Environmental Engineering, The University of Texas at Austin, 301 East Dean Keeton St., Stop C1747, Austin, TX 78712, U.S.A.
†E-mail: loukas@mail.utexas.edu

Post-earthquake observations of oil production at depleted oil fields [2–6] and a few field experiments [7–12] suggest that stress wave stimulation of oil reservoirs (geological formations) may lead to the expulsion of particles trapped in their interstices. Many researchers have conducted analytical and laboratory investigations of the underlying physical phenomenon to establish the mechanisms responsible for the vibratory mobilization of trapped oil or colloidal particles. These studies [7, 8, 13–23] suggest that (a) stress wave stimulation of geological formations can aid the expulsion of particles trapped in their pore space, provided that the wave motion exceeds the mobilization threshold and (b) an estimate of the mobilization threshold can be obtained by conducting analytical and laboratory investigations. Based on the field and laboratory observations, it was conjectured [7, 8, 24, 25] that stress wave stimulation of geological formations can provide a primary or auxiliary recourse for enhanced oil recovery. In the, so-called, wave-based EOR method, the stress wave stimulation is applied using artificial wave sources (e.g., a fleet of Vibroseis and down-hole hydraulic pumps). The effectiveness of the stimulation is contingent upon, among other factors, the strength and spatial extent of the wave motion in the oil reservoir. Thus, a successful field implementation of the said EOR method requires (a) an estimate of the strength (magnitude) of the wave motion that facilitates the removal of trapped oil from the reservoir and (b) an efficient wave energy delivery system to generate the wave motion of the required magnitude in the reservoir. When artificial wave sources are used to initiate the wave motion, equipment limitations and various sources of attenuation impose restrictions on the magnitude of the wave motion generated in the target formation. Therefore, blindly operating sources may not be able to breach the threshold of motion required for particle expulsion, or they may not deliver the stress wave stimulation in a technically and economically efficient manner. Thus, a cost-effective field implementation of the wave-based EOR method necessitates selection of *advantageous* or *optimal* spatio-temporal characteristics of the wave sources. In this article, we discuss an optimization-based algorithm for designing an efficient wave energy delivery system.

If the material and geometric description of the geostructure in question and the capabilities (maximum amplitude, frequency range, etc.) of the wave sources are known, then the spatio-temporal source characteristics that focus the wave energy into the target formation can be computed using reservoir-scale wave physics simulations. For example, if the locations of the sources are (assumed to be) fixed, then a frequency sweep could be used to determine the dominant frequency of monochromatic time signals driving the sources. The frequency sweep method uses a mathematical model of the wave physics to compute a predefined motion metric of the target formation for a range of frequencies. The frequency corresponding to the maximum value of the metric can be used to design time signals that drive the sources. However, when advantageous source locations are also required, a combined frequency-and-location sweep becomes computationally prohibitive. Another approach for focusing the wave energy into the target formation is based on the principle of time reversal [26–30]. It involves (a) placing a source in the target formation; (b) recording the waves emitted by this source at sensors placed on the boundary of the domain (the ground surface); and (c) re-transmitting the time-reversed versions of the recorded signals from their respective sensor locations. Although, under favorable conditions, the time-reversed signals could focus at the target, the methodology does not ensure maximization of a motion metric of the target zone.

Alternatively, the spatio-temporal characteristics of the wave sources that maximize a predefined motion metric of the target inclusion can be computed using an optimization-based scheme. This approach formally gives rise to an inverse source problem, which is similar to the inverse medium problems arising in exploration geophysics [31–37]. Jeong *et al.* used the inverse source approach to compute the optimal time signals driving the surface sources for a geostructure abstracted as a layered elastic solid in one or two spatial dimensions [38–40], whereas Karve *et al.* [41, 42] developed an inverse source methodology to resolve not only the optimal source signals but also the optimal source locations. They conducted numerical experiments for two-dimensional (2D), synthetically created geostructures and reported that the optimal source locations play a crucial role in maximizing wave energy delivery to the target formation.

The preceding developments are restricted to two spatial dimensions. Herein, we extend the development to the all-important three-dimensional case. As the radiation damping is much more severe in three spatial dimensions, realistic estimates of the required surface energy and of the

energy delivered to the target formation require the resolution of the inverse source problem in three dimensions. Although the methodology in three dimensions is similar to the two-dimensional development, there are various differences at the modeling level that require algorithmic modifications. Thus, in this article, we formulate and resolve the wave energy delivery inverse source problem for a three-dimensional, elastic, heterogeneous, semi-infinite solid. We truncate the semi-infinite domain of interest using a buffer of hybrid perfectly matched layers (PMLs) [43]. Our working hypotheses are (a) the material properties and the overall geometry of the target formation and the surrounding geostructure are known and (b) the stress waves are initiated by surface sources (e.g., a fleet of Vibroseis). We remark that the methodology can also be used to decide the optimal locations and frequency content of down-hole wave sources. We cast the inverse source problem as a constrained minimization problem, where minimization of a suitably defined objective functional is tantamount to the maximization of a motion metric of the target formation and the governing wave physics equations are side-imposed as constraints. In the following sections, we discuss the formulation of the forward wave propagation problem, the inverse source problem, the numerical implementation, and report the results of our numerical experiments conducted using a synthetically created geo-formation that affirms the ability of the proposed optimization methodology to yield source characteristics that lead to wave energy focusing.

   Although the development is motivated by a problem arising in exploration geophysics or petroleum engineering, the methodology is equally applicable to medical applications where optimal energy delivery is of interest for therapeutic reasons.

2. THE FORWARD PROBLEM

2.1. Strong form

We are concerned with stress wave propagation in a three-dimensional, heterogeneous, elastic half-space containing a target inclusion. In order to obtain a finite computational model, we truncate the domain of interest ($\Omega_{\text{reg}} = \Omega_{\text{a}} \cup \Omega_{\text{b}}$) using hybrid PMLs ($\Omega_{\text{PML}}$) [43]. Note that in Figure 1, Ω_{a} represents the target inclusion and Ω_{b} represents the heterogeneous elastic solid surrounding the target inclusion. The governing equations in $\Omega = \Omega_{\text{reg}} \cup \Omega_{\text{PML}}$, for time $t \in \text{J} = (0, T]$, are given as

$$\mathbf{div}\left[\mu_{\text{a}}\left(\nabla \dot{\mathbf{u}}_{\text{a}} + \nabla \dot{\mathbf{u}}_{\text{a}}^{T}\right) + \left(\lambda_{\text{a}} \operatorname{div} \dot{\mathbf{u}}_{\text{a}}\right)\mathbf{I}\right] - \rho_{\text{a}}\ddot{\mathbf{u}}_{\text{a}} = \mathbf{0}, \mathbf{x} \in \Omega_{\text{a}} \tag{1}$$
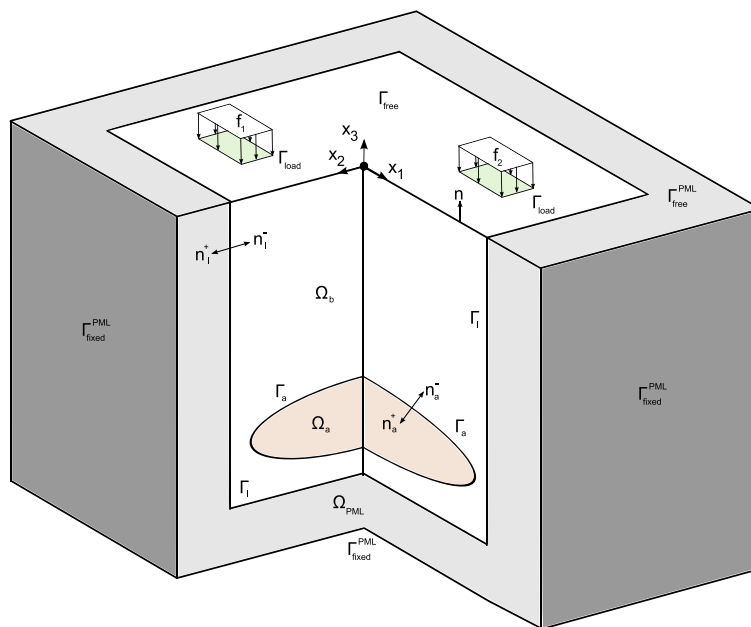

Figure 1. Problem definition. [Colour figure can be viewed at wileyonlinelibrary.com]

Table I. Symbols used to represent the displacement
field and the material properties.

	Ω_a	$\Omega_b \cup \Omega_{PML}$
Displacement field	$\mathbf{u}_a$	$\mathbf{u}_b$
First Lamé parameter	λ_a	λ_b
Second Lamé parameter	μ_a	μ_b
Mass density	ρ_a	ρ_b

and

$$\mathbf{div}\left[\mu_b\left(\nabla\dot{\mathbf{u}}_b + \nabla\dot{\mathbf{u}}_b^T\right) + (\lambda_b\,\mathrm{div}\,\dot{\mathbf{u}}_b)\,\mathbf{I}\right] - \rho_b\ddot{\mathbf{u}}_b = \mathbf{0}, \mathbf{x}\in\Omega_b, \tag{2a}$$

$$\mathbf{div}\left(\ddot{\mathbf{S}}^T\Lambda_e + \dot{\mathbf{S}}^T\Lambda_p + \mathbf{S}^T\Lambda_w\right) - \rho_b\left(a\dddot{\mathbf{u}}_b + b\ddot{\mathbf{u}}_b + c\dot{\mathbf{u}}_b + d\mathbf{u}_b\right) = \mathbf{0}, \mathbf{x}\in\Omega_{PML}, \tag{2b}$$

$$(a\dddot{\mathbf{S}} + b\ddot{\mathbf{S}} + c\dot{\mathbf{S}} + d\mathbf{S}) - \lambda_b(\mathrm{div}(\Lambda_e\ddot{\mathbf{u}}_b) + \mathrm{div}(\Lambda_p\dot{\mathbf{u}}_b) + \mathrm{div}(\Lambda_w\mathbf{u}_b))$$
$$-\mu_b\left[\nabla\ddot{\mathbf{u}}_b\Lambda_e + \Lambda_e(\nabla\ddot{\mathbf{u}}_b)^T + \nabla\dot{\mathbf{u}}_b\Lambda_p + \Lambda_p(\nabla\dot{\mathbf{u}}_b)^T + \nabla\mathbf{u}_b\Lambda_w + \Lambda_w(\nabla\mathbf{u}_b)^T\right] = \mathbf{0}, \mathbf{x}\in\Omega_{PML}, \tag{2c}$$

where an overdot, ($\dot{}$), denotes a derivative with respect to time. The higher-order time derivatives in Equations (1) and (2) are required in order to facilitate the adoption of PMLs at the truncation boundary [43]. Equations (1), (2a), and (2b) are the equilibrium equations for Ω_a, Ω_b, and Ω_{PML}, respectively. Equation (2c) is the combined kinematic condition and constitutive law for the PML region (Ω_{PML}). Various symbols used to denote the displacement vectors and the material properties are explained in Table I.

In Equation (2), $\mathbf{S}$ is the stress *history* tensor, that is,

$$\mathbf{S}(\mathbf{x},t) = \begin{bmatrix} \mathbf{S}_{11}(\mathbf{x},t) & \mathbf{S}_{12}(\mathbf{x},t) & \mathbf{S}_{13}(\mathbf{x},t) \\ \mathbf{S}_{21}(\mathbf{x},t) & \mathbf{S}_{22}(\mathbf{x},t) & \mathbf{S}_{23}(\mathbf{x},t) \\ \mathbf{S}_{31}(\mathbf{x},t) & \mathbf{S}_{32}(\mathbf{x},t) & \mathbf{S}_{33}(\mathbf{x},t) \end{bmatrix} = \int_0^t \boldsymbol{\sigma}(\mathbf{x},t')dt', \tag{3}$$

where $\boldsymbol{\sigma}$ is the Cauchy stress tensor. Λ_e, Λ_p, and Λ_w are components of the stretching tensor, and a, b, c, d are coefficients defining co-ordinate stretching in the PML region. Their detailed definitions are beyond the scope of this article and can be found in [43]. For $t \in J$, the governing equations are subjected to the following boundary conditions:

$$\mathbf{u}_b = \mathbf{0}, \mathbf{x}\in\Gamma_{\text{fixed}}^{\text{PML}}, \tag{4a}$$

$$\left[\mu_b\left(\nabla\dot{\mathbf{u}}_b + \nabla\dot{\mathbf{u}}_b^T\right) + \{\lambda_b\,\mathrm{div}\,\dot{\mathbf{u}}_b\}\,\mathbf{I}\right]\mathbf{n} = \dot{\mathbf{f}}, \mathbf{x}\in\Gamma_{\text{load}}, \tag{4b}$$

$$\left[\mu_b\left(\nabla\dot{\mathbf{u}}_b + \nabla\dot{\mathbf{u}}_b^T\right) + \{\lambda_b\,\mathrm{div}\,\dot{\mathbf{u}}_b\}\,\mathbf{I}\right]\mathbf{n} = \mathbf{0}, \mathbf{x}\in\Gamma_{\text{free}}, \tag{4c}$$

$$\left(\ddot{\mathbf{S}}^T\Lambda_e + \dot{\mathbf{S}}^T\Lambda_p + \mathbf{S}^T\Lambda_w\right)\mathbf{n} = \mathbf{0}, \mathbf{x}\in\Gamma_{\text{free}}^{\text{PML}}, \tag{4d}$$

$$\mathbf{u}_b^+ = \mathbf{u}_b^-, \mathbf{x}\in\Gamma_I, \tag{4e}$$

$$\left[\mu_b\left(\nabla\dot{\mathbf{u}}_b + \nabla\dot{\mathbf{u}}_b^T\right) + \{\lambda_b\,\mathrm{div}\,\dot{\mathbf{u}}_b\}\,\mathbf{I}\right]\mathbf{n}_I^+ = -\left(\ddot{\mathbf{S}}^T\Lambda_e + \dot{\mathbf{S}}^T\Lambda_p + \mathbf{S}^T\Lambda_w\right)\mathbf{n}_I^-, \mathbf{x}\in\Gamma_I; \tag{4f}$$

interface conditions:

$$\mathbf{u}_a = \mathbf{u}_b, \mathbf{x}\in\Gamma_a, \tag{5a}$$

$$\boldsymbol{\sigma}_a^T\mathbf{n}_a^- = -\boldsymbol{\sigma}_b^T\mathbf{n}_a^+, \mathbf{x}\in\Gamma_a; \tag{5b}$$

$$\text{where,}\ \boldsymbol{\sigma}_a = \mu_a\left(\nabla\mathbf{u}_a + \nabla\mathbf{u}_a^T\right) + \lambda_a(\mathrm{div}\,\mathbf{u}_a)\mathbf{I}, \tag{5c}$$

$$\boldsymbol{\sigma}_b = \mu_b\left(\nabla\mathbf{u}_b + \nabla\mathbf{u}_b^T\right) + \lambda_b(\mathrm{div}\mathbf{u}_b)\mathbf{I}; \tag{5d}$$

and initial value conditions:

$$\mathbf{u}(\mathbf{x},0) = \mathbf{0}, \quad \dot{\mathbf{u}}(\mathbf{x},0) = \mathbf{0}, \qquad \mathbf{x} \in \Omega, \tag{6a}$$

$$\mathbf{S}(\mathbf{x},0) = \mathbf{0}, \quad \dot{\mathbf{S}}(\mathbf{x},0) = \mathbf{0}, \qquad \mathbf{x} \in \Omega_{\text{PML}}. \tag{6b}$$

Thus, the forward wave propagation problem is concerned with computing the displacement (velocity and acceleration) field in the domain of interest, given the applied loads and the material properties of the heterogeneous halfspace. We intend to use spectral elements to resolve the forward wave propagation problem. To this end, we formulate the problem in its weak form.

2.2. Weak form

We take an inner product between the test functions $\mathbf{v}_a(\mathbf{x})$, $\mathbf{v}_b(\mathbf{x})$, and the equilibrium Equations (1), (2a), and (2b), integrate over their respective domains, and add them. We take another inner product between the test function $\mathbf{T}(\mathbf{x})$ and Equation (2c) and integrate over Ω_{PML}. After some simplifications, we arrive at the following integral equations:

$$\int_{\Omega_a} \nabla \mathbf{v}_a : \left[\mu_a \left(\nabla \dot{\mathbf{u}}_a + \nabla \dot{\mathbf{u}}_a^T \right) + \lambda_a \, (\text{div } \dot{\mathbf{u}}_a)\mathbf{I} \right] + \mathbf{v}_a \cdot \rho_a \ddot{\mathbf{u}}_a \, d\Omega$$

$$+ \int_{\Omega_b} \nabla \mathbf{v}_b : \left[\mu_b(\nabla \dot{\mathbf{u}}_b + \nabla \dot{\mathbf{u}}_b^T) + \lambda_b \, (\text{div } \dot{\mathbf{u}}_b)\mathbf{I} \right] + \mathbf{v}_b \cdot \rho_b \ddot{\mathbf{u}}_b \, d\Omega$$

$$+ \int_{\Omega_{\text{PML}}} \nabla \mathbf{v}_b : \left(\ddot{\mathbf{S}}^T \Lambda_e + \dot{\mathbf{S}}^T \Lambda_p + \mathbf{S}^T \Lambda_w \right) + \mathbf{v}_b \cdot \rho_b \, (\text{a}\ddot{\mathbf{u}}_b + \text{b}\ddot{\mathbf{u}}_b + \text{c}\dot{\mathbf{u}}_b + \text{d}\mathbf{u}_b) \, d\Omega = \int_{\Gamma_{\text{load}}} \mathbf{v}_b \cdot \dot{\mathbf{f}} \, d\Gamma \tag{7a}$$

$$\int_{\Omega_{\text{PML}}} \mathbf{T} : \Big\{ (\text{a}\ddot{\mathbf{S}} + \text{b}\ddot{\mathbf{S}} + \text{c}\dot{\mathbf{S}} + \text{d}\mathbf{S}) - \lambda_b(\text{div}(\Lambda_e \ddot{\mathbf{u}}_b) + \text{div}(\Lambda_p \dot{\mathbf{u}}_b) + \text{div}(\Lambda_w \mathbf{u}_b)) \tag{7b}$$

$$-\mu_b \left[\nabla \ddot{\mathbf{u}}_b \Lambda_e + \Lambda_e (\nabla \ddot{\mathbf{u}}_b)^T + \nabla \dot{\mathbf{u}}_b \Lambda_p + \Lambda_p (\nabla \dot{\mathbf{u}}_b)^T + \nabla \mathbf{u}_b \Lambda_w + \Lambda_w (\nabla \mathbf{u}_b)^T \right] \Big\} \, d\Omega = 0,$$

where a colon, (:), represents tensor inner product. The weak form of the forward problem can be stated as given loads $\mathbf{f}(\mathbf{x},t) \in \mathbf{L}^2(\Omega_{\text{reg}}) \times \text{J}$, find $\mathbf{u}_a(\mathbf{x},t) \in \mathbf{H}^1(\Omega_a) \times \text{J}$, $\mathbf{u}_b(\mathbf{x},t) \in \mathbf{H}^1(\Omega_b \cup \Omega_{\text{PML}}) \times \text{J}$, and $\mathbf{S}(\mathbf{x},t) \in \mathcal{L}^2(\Omega_{\text{PML}}) \times \text{J}$, so that they satisfy Equation (7) and condition (6), for every $\mathbf{v}_a(\mathbf{x}) \in \mathbf{H}^1(\Omega_a)$, $\mathbf{v}_b(\mathbf{x}) \in \mathbf{H}^1(\Omega_b \cup \Omega_{\text{PML}})$, and $\mathbf{T}(\mathbf{x}) \in \mathcal{L}^2(\Omega_{\text{PML}})$. The pertinent function spaces for a scalar f, a vector $\mathbf{u}$, and a tensor $\mathbf{T}$ are given by

$$L^2(\Omega) = \{ f : \int_{\Omega} |f|^2 d\Omega < \infty \}, \tag{8a}$$

$$\mathbf{L}^2(\Omega) = \{ \mathbf{u} : \mathbf{u} \in (L^2(\Omega))^3 \}, \tag{8b}$$

$$\mathcal{L}^2(\Omega) = \{ \mathbf{T} : \mathbf{T} \in (L^2(\Omega))^{3\times 3} \}, \tag{8c}$$

$$H^1(\Omega) = \{ f : \int_{\Omega} (|f|^2 + |\nabla f|^2) d\Omega < \infty, \, f(\mathbf{x}) = 0 \text{ if } \mathbf{x} \in \Gamma_{\text{fixed}}^{\text{PML}} \}, \tag{8d}$$

$$\mathbf{H}^1(\Omega) = \{ \mathbf{u} : \mathbf{u} \in (H^1(\Omega))^3 \}. \tag{8e}$$

2.3. Spatial discretization and the semi-discrete form

Numerical solution of the weak form requires discretization in space and time. We introduce spatial discretization using shape functions $\mathbf{\Phi}(\mathbf{x}) \in \mathbf{H}_h^1(\Omega) \subset \mathbf{H}^1(\Omega)$ and $\mathbf{\Psi}(\mathbf{x}) \in \mathcal{L}_h^2(\Omega_{\text{PML}}) \subset \mathcal{L}^2(\Omega_{\text{PML}})$.

Thus, the discrete approximations for the test functions are given by

$$
\mathbf{v}_a^h(\mathbf{x}) = \begin{bmatrix} \mathbf{v}_{a_1}^T \boldsymbol{\Phi}(\mathbf{x}) \\ \mathbf{v}_{a_2}^T \boldsymbol{\Phi}(\mathbf{x}) \\ \mathbf{v}_{a_3}^T \boldsymbol{\Phi}(\mathbf{x}) \end{bmatrix}, \mathbf{v}_b^h(\mathbf{x}) = \begin{bmatrix} \mathbf{v}_{b_1}^T \boldsymbol{\Phi}(\mathbf{x}) \\ \mathbf{v}_{b_2}^T \boldsymbol{\Phi}(\mathbf{x}) \\ \mathbf{v}_{b_3}^T \boldsymbol{\Phi}(\mathbf{x}) \end{bmatrix},
$$
$$
\mathbf{T}^h(\mathbf{x}) = \begin{bmatrix} T_{11}^T \boldsymbol{\Psi}(\mathbf{x}) & T_{12}^T \boldsymbol{\Psi}(\mathbf{x}) & T_{13}^T \boldsymbol{\Psi}(\mathbf{x}) \\ T_{21}^T \boldsymbol{\Psi}(\mathbf{x}) & T_{22}^T \boldsymbol{\Psi}(\mathbf{x}) & T_{23}^T \boldsymbol{\Psi}(\mathbf{x}) \\ T_{31}^T \boldsymbol{\Psi}(\mathbf{x}) & T_{32}^T \boldsymbol{\Psi}(\mathbf{x}) & T_{33}^T \boldsymbol{\Psi}(\mathbf{x}) \end{bmatrix},
\tag{9}
$$

where the vectors $\mathbf{v}_{a_i}, \mathbf{v}_{b_i}$, and $\mathbf{T}_{ij}$ contain the nodal values of the test functions. Similarly, the approximants for the trial solutions are given by

$$
\mathbf{u}_a^h(\mathbf{x}, t) = \begin{bmatrix} \boldsymbol{\Phi}(\mathbf{x})^T \mathbf{u}_{a_1}(t) \\ \boldsymbol{\Phi}(\mathbf{x})^T \mathbf{u}_{a_2}(t) \\ \boldsymbol{\Phi}(\mathbf{x})^T \mathbf{u}_{a_3}(t) \end{bmatrix}, \mathbf{u}_b^h(\mathbf{x}, t) = \begin{bmatrix} \boldsymbol{\Phi}(\mathbf{x})^T \mathbf{u}_{b_1}(t) \\ \boldsymbol{\Phi}(\mathbf{x})^T \mathbf{u}_{b_2}(t) \\ \boldsymbol{\Phi}(\mathbf{x})^T \mathbf{u}_{b_3}(t) \end{bmatrix},
$$
$$
\mathbf{S}^h(\mathbf{x}, t) = \begin{bmatrix} \boldsymbol{\Psi}(\mathbf{x})^T S_{11}(t) & \boldsymbol{\Psi}(\mathbf{x})^T S_{12}(t) & \boldsymbol{\Psi}(\mathbf{x})^T S_{13}(t) \\ \boldsymbol{\Psi}(\mathbf{x})^T S_{21}(t) & \boldsymbol{\Psi}(\mathbf{x})^T S_{22}(t) & \boldsymbol{\Psi}(\mathbf{x})^T S_{23}(t) \\ \boldsymbol{\Psi}(\mathbf{x})^T S_{31}(t) & \boldsymbol{\Psi}(\mathbf{x})^T S_{32}(t) & \boldsymbol{\Psi}(\mathbf{x})^T S_{33}(t) \end{bmatrix},
\tag{10}
$$

where the vectors $\mathbf{u}_{a_i}(t), \mathbf{u}_{b_i}(t)$, and $S_{ij}(t)$ contain the nodal values of the variables at time t. Introducing the approximations (Equations (9) and (10)) into Equation (7) yields the following semi-discrete form:

$$
\mathbf{M}\ddot{\mathbf{d}} + \mathbf{C}\dot{\mathbf{d}} + \mathbf{K}\dot{\mathbf{d}} + \mathbf{G}\mathbf{d} = \dot{\mathbf{F}},
\tag{11}
$$

where

$$
\mathbf{d} = [\mathbf{u}_{a_1} \mathbf{u}_{a_2} \mathbf{u}_{a_3} \big| \mathbf{u}_{b_1} \mathbf{u}_{b_2} \mathbf{u}_{b_3} \big| S_{11} S_{12} \ldots S_{33}]^T = [\tilde{\mathbf{u}}_a \big| \tilde{\mathbf{u}}_b \big| \tilde{\mathbf{S}}]^T,
\tag{12}
$$

$$
\mathbf{F} = [\mathbf{0} \big| F_1 \ F_2 \ F_3 \big| \mathbf{0}]^T,
\tag{13}
$$

and the temporal dependencies have been suppressed for brevity. In Equation (11), $\mathbf{M}, \mathbf{C}, \mathbf{K}$, and $\mathbf{G}$ are the global system matrices. They can be computed given the values of the Lamé parameters and mass densities in the heterogeneous domain (Ω_{reg}) and the parameters defining coordinate stretching in the PML region (Ω_{PML}). Detailed definitions of the system matrices and their constituent element matrices can be found in [43]. We remark that the matrix $\mathbf{G}$ has zero elements everywhere except in the PML region. Thus, the matrix-vector product $\mathbf{G}\mathbf{d}$ is nonzero only in Ω_{PML}. Next, we discuss the time integration of the semi-discrete form (11).

2.4. Temporal discretization and integration

Various schemes for integrating the system of third-order ordinary differential equations (ODEs, Equation 11) in time have been discussed in [43]. Here, we favor an explicit time integration scheme that requires recasting the semi-discrete form as a system of first-order ODEs in time. To this end, we (analytically) integrate Equation (11) in time to obtain a system of second-order ODEs given by

$$
\mathbf{M}\ddot{\mathbf{d}} + \mathbf{C}\dot{\mathbf{d}} + \mathbf{K}\mathbf{d} + \mathbf{G}\tilde{\mathbf{d}} = \mathbf{F}, \quad \dot{\tilde{\mathbf{d}}} = \mathbf{d}|_{\text{PML}},
\tag{14}
$$

where we have assumed silent initial conditions and $\tilde{\mathbf{d}}$ contains the displacement and stress history degrees-of-freedom within Ω_{PML} only [43]. Equation (14) can be expressed as a first-order system

in time, as

$$\mathbf{A}\dot{\mathbf{y}} = \mathbf{B}\mathbf{y} + \mathbf{D}, \tag{15a}$$

where $\tag{15b}$

$$\mathbf{y} = [\mathbf{z}_0 \ \mathbf{z}_1 \ \mathbf{z}_2]^T, \mathbf{z}_0 = \tilde{\mathbf{d}}, \mathbf{z}_1 = \mathbf{d}, \mathbf{z}_2 = \dot{\mathbf{d}}, \tag{15c}$$

$$\mathbf{A} = \begin{bmatrix} \mathbf{I} & 0 & 0 \\ 0 & \mathbf{I} & 0 \\ 0 & 0 & \mathbf{M} \end{bmatrix}, \mathbf{B} = \begin{bmatrix} 0 & \mathbf{I} & 0 \\ 0 & 0 & \mathbf{I} \\ -\mathbf{G} & -\mathbf{K} & -\mathbf{C} \end{bmatrix}, \text{ and } \mathbf{D} = \begin{bmatrix} 0 \\ 0 \\ \mathbf{F} \end{bmatrix}. \tag{15d}$$

An explicit scheme can be used to solve (15) if the inverse of $\mathbf{A}$ (i.e., the mass-like matrix, $\mathbf{M}$) can be computed efficiently. This can be achieved if the mass-like matrix $\mathbf{M}$ is diagonal. To obtain a diagonal matrix $\mathbf{M}$, we use spectral elements for spatial discretization and employ the Legendre–Gauss–Lobatto quadrature rule for computing the system matrices. Now, Equation (15) can be rewritten as

$$\dot{\mathbf{y}} = \mathbf{L}\mathbf{y} + \mathbf{R}, \qquad \text{where} \tag{16a}$$

$$\mathbf{L} = \begin{bmatrix} 0 & \mathbf{I} & 0 \\ 0 & 0 & \mathbf{I} \\ -\hat{\mathbf{G}} & -\hat{\mathbf{K}} & -\hat{\mathbf{C}} \end{bmatrix}, \mathbf{R} = \begin{bmatrix} 0 \\ 0 \\ \hat{\mathbf{F}} \end{bmatrix}, \tag{16b}$$

$$\hat{\mathbf{C}} = \mathbf{M}^{-1}\mathbf{C}, \qquad \hat{\mathbf{K}} = \mathbf{M}^{-1}\mathbf{K}, \qquad \hat{\mathbf{G}} = \mathbf{M}^{-1}\mathbf{G}, \qquad \hat{\mathbf{F}} = \mathbf{M}^{-1}\mathbf{F}, \tag{16c}$$

and the inverse of the mass-like matrix ($\mathbf{M}^{-1}$) can be easily computed by taking the reciprocals of the diagonal entries.

The temporal dimension is now discretized using a timestep τ. The value of a variable at the i-th timestep is denoted by superscript 'i', that is, $\mathbf{y}^i \equiv \mathbf{y}(t)$ at $t = i \ \tau$. We employ the fourth-order Runge–Kutta (RK4) scheme for time integration of Equation (16a). Using this method, $\mathbf{y}^{i+1}$ can be computed using $\mathbf{y}^i$ as

$$\mathbf{y}^{i+1} = \mathbf{y}^i + \frac{\tau}{6}\left[\mathbf{H}_1^i + 2\mathbf{H}_2^i + 2\mathbf{H}_3^i + \mathbf{H}_4^i\right], \tag{17}$$

where $\mathbf{H}_k^i = [\mathbf{h}_{k0}^i \ \mathbf{h}_{k1}^i \ \mathbf{h}_{k2}^i]^T$ and

$$\mathbf{h}_{10}^i = \mathbf{z}_1^i, \tag{18a}$$

$$\mathbf{h}_{11}^i = \mathbf{z}_2^i, \tag{18b}$$

$$\mathbf{h}_{12}^i = -\hat{\mathbf{C}}\mathbf{z}_2^i - \hat{\mathbf{K}}\mathbf{z}_1^i - \hat{\mathbf{G}}\mathbf{z}_0^i - \hat{\mathbf{F}}^i, \tag{18c}$$

$$\mathbf{h}_{20}^i = \mathbf{z}_1^i + \frac{\tau}{2}\mathbf{h}_{11}^i, \tag{18d}$$

$$\mathbf{h}_{21}^i = \mathbf{z}_2^i + \frac{\tau}{2}\mathbf{h}_{12}^i, \tag{18e}$$

$$\mathbf{h}_{22}^i = -\hat{\mathbf{C}}(\mathbf{z}_2^i + \frac{\tau}{2}\mathbf{h}_{12}^i) - \hat{\mathbf{K}}(\mathbf{z}_1^i + \frac{\tau}{2}\mathbf{h}_{11}^i) - \hat{\mathbf{G}}(\mathbf{z}_0^i + \frac{\tau}{2}\mathbf{h}_{10}^i) - \hat{\mathbf{F}}^{i+\frac{1}{2}}, \tag{18f}$$

$$\mathbf{h}_{30}^i = \mathbf{z}_1^i + \frac{\tau}{2}\mathbf{h}_{21}^i, \tag{18g}$$

$$\mathbf{h}_{31}^i = \mathbf{z}_2^i + \frac{\tau}{2}\mathbf{h}_{22}^i, \tag{18h}$$

$$\mathbf{h}_{32}^i = -\hat{\mathbf{C}}(\mathbf{z}_2^i + \frac{\tau}{2}\mathbf{h}_{22}^i) - \hat{\mathbf{K}}(\mathbf{z}_1^i + \frac{\tau}{2}\mathbf{h}_{21}^i) - \hat{\mathbf{G}}(\mathbf{z}_0^i + \frac{\tau}{2}\mathbf{h}_{20}^i) - \hat{\mathbf{F}}^{i+\frac{1}{2}}, \tag{18i}$$

$$\mathbf{h}_{40}^i = \mathbf{z}_1^i + \tau\mathbf{h}_{31}^i, \tag{18j}$$

$$\mathbf{h}_{41}^i = \mathbf{z}_2^i + \tau\mathbf{h}_{32}^i, \tag{18k}$$

$$\mathbf{h}_{42}^i = -\hat{\mathbf{C}}(\mathbf{z}_2^i + \tau\mathbf{h}_{32}^i) - \hat{\mathbf{K}}(\mathbf{z}_1^i + \tau\mathbf{h}_{31}^i) - \hat{\mathbf{G}}(\mathbf{z}_0^i + \tau\mathbf{h}_{30}^i) - \hat{\mathbf{F}}^{i+1}. \tag{18l}$$

Thus, Equations (17) and (18) can be used to compute the displacement ($\dot{\mathbf{z}}_0$), velocity ($\dot{\mathbf{z}}_1$), and acceleration ($\dot{\mathbf{z}}_2$) vectors at the $(i + 1)$-th timestep given their values at the i-th timestep and the

force vector **F**. The step-by-step time marching scheme can be represented as a solution of linear system of equations given by

$$Qu = f, \tag{19}$$

where

$$u = [\mathbf{y}^0 \,|\, \mathbf{H}_1^0 \, \mathbf{H}_2^0 \, \mathbf{H}_3^0 \, \mathbf{H}_4^0 \,|\, \mathbf{y}^1 \,|\, \mathbf{H}_1^1 \, \mathbf{H}_2^1 \, \mathbf{H}_3^1 \, \mathbf{H}_4^1 \,|\, \mathbf{y}^2 \,|\, \cdots \, \mathbf{H}_1^{N-1} \, \mathbf{H}_2^{N-1} \, \mathbf{H}_3^{N-1} \, \mathbf{H}_4^{N-1} \,|\, \mathbf{y}^N \,]^T, \tag{20}$$

$$f = [\mathbf{y}_0 \,|\, \mathbf{R}^0 \, \mathbf{R}^{\frac{1}{2}} \, \mathbf{R}^{\frac{1}{2}} \, \mathbf{R}^1 \,|\, \mathbf{0} \,|\, \mathbf{R}^1 \, \mathbf{R}^{1\frac{1}{2}} \, \mathbf{R}^{1\frac{1}{2}} \, \mathbf{R}^2 \,|\, \mathbf{0} \,|\, \cdots \, \mathbf{R}^{N-1} \, \mathbf{R}^{N-\frac{1}{2}} \, \mathbf{R}^{N-\frac{1}{2}} \, \mathbf{R}^N \,|\, \mathbf{0} \,]^T, \tag{21}$$

and the matrix Q is given in Appendix A.

3. LOAD MODELING

In the inverse source problem, the source time signals and source locations are treated as unknowns. The spatio-temporal source characteristics that maximize a specified motion metric of the target formation are computed using an iterative procedure. This necessitates parameterization of the spatial and temporal load descriptors. Specifically, the tractions $\mathbf{f}(\mathbf{x}, t)$ applied on Γ_{load} consist of contributions, $\mathbf{f}_i(\mathbf{x}, t)$, from n_s sources. The i-th source is defined using a spatial ($\boldsymbol{\theta}_i(\mathbf{x})$) and a temporal ($f_i(t)$) component. $\boldsymbol{\theta}_i$ is further decomposed into x_p-directional components: $\theta_{ip}(\mathbf{x})$, $p = 1, 2, 3$. Thus,

$$\mathbf{f}(\mathbf{x}, t) = \sum_{i=1}^{n_s} \mathbf{f}_i(\mathbf{x}, t) = \sum_{i=1}^{n_s} \begin{bmatrix} \theta_{i1}(\mathbf{x}) \\ \theta_{i2}(\mathbf{x}) \\ \theta_{i3}(\mathbf{x}) \end{bmatrix} f_i(t). \tag{22}$$

In our numerical experiments, we apply loads in either x_1, x_2, or x_3 direction; therefore, $\theta_{ip}(\mathbf{x}) \neq 0$ for only a single value of p. The spatial variation of the i-th load on Γ_{load} is captured by θ_{ip}, for example, a constant pressure load applied on part of the surface ($x_3 = 0$) can be expressed as

$$\theta_{ip}(x_1, x_2, 0) = \left[H\left(\eta_{i1} - \frac{b_{i1}}{2}\right) - H\left(\eta_{i1} + \frac{b_{i1}}{2}\right) \right] \cdot \left[H\left(\eta_{i2} - \frac{b_{i2}}{2}\right) - H\left(\eta_{i2} + \frac{b_{i2}}{2}\right) \right], \tag{23}$$

where H is the Heaviside step function, η_{ik} ($k = 1, 2$) are the (unknown) x_k coordinates of the i-th load's centerline, and b_{ik} is the width of the load along the x_k-direction. Similarly, a load varying like the Gaussian function is given by

$$\theta_{ip}(x_1, x_2, 0) = \exp\left[\frac{-(x_1 - \eta_{i1})^2}{b_{i1}} \right] \exp\left[\frac{-(x_2 - \eta_{i2})^2}{b_{i2}} \right]. \tag{24}$$

We parameterize the time signals using quadratic Lagrange polynomials $\phi_j(t)$ whose temporal nodal values are denoted by ξ_{ij}. This allows us to express $f_i(t)$ as

$$f_i(t) = \sum_{j=1}^{n_f} \xi_{ij} \phi_j(t), \tag{25}$$

where n_f is the number of Lagrange polynomials used to define the time signal. Next, we cast the inverse source problem aimed at focusing wave energy into the target formation.

4. THE INVERSE SOURCE PROBLEM

The inverse source problem aims at maximization of a motion metric of the target formation by seeking the optimal spatio-temporal source characteristics. The problem can be cast as a constrained minimization problem, wherein an objective functional is minimized while staying within the constraints imposed by the governing physics. The objective functional and the constraint conditions defined either in the continuous (strong or weak) form or in the spatio-temporally discretized form can be used to formulate the inverse source problem [41, 44, 45]. In this work, we favor the latter approach. We cast the discrete objective functional as

$$\mathcal{L}_d = \frac{1}{\boldsymbol{u}^T \mathbf{B}_{\dot{u}_a} \boldsymbol{u}} = \frac{1}{\tau \left[\frac{1}{2} \dot{\tilde{u}}_a^0 \cdot \dot{\tilde{u}}_a^0 + \frac{1}{2} \dot{\tilde{u}}_a^N \cdot \dot{\tilde{u}}_a^N + \sum_{i=1}^{N-1} \dot{\tilde{u}}_a^i \cdot \dot{\tilde{u}}_a^i \right]}, \tag{26}$$

where the vector of nodal velocities in the target inclusion, $\dot{\tilde{u}}_a^i$, is formally defined in Equation (12) and $\boldsymbol{B}_{\dot{u}_a}$ is a block diagonal matrix with $\tau \mathbf{B}_i$ on its diagonals. $\mathbf{B}_i$ are square matrices that are zero everywhere except on diagonals that correspond to the elements of $\dot{\tilde{u}}_a^i$. Minimization of $\mathcal{L}_d$ is tantamount to the maximization of the velocity field within the target inclusion. Next, we form the augmented functional and obtain the first-order optimality conditions.

4.1. The augmented functional

We side-impose the governing Equation (19), weighted by the discrete Lagrange multipliers $\boldsymbol{p}$, on the objective functional to obtain the discrete augmented functional which is to be minimized. Thus, the inverse problem can now be stated as

$$\min_{\boldsymbol{f}} \ \mathcal{A}(\boldsymbol{u}, \boldsymbol{p}, \boldsymbol{f}) = \mathcal{L}_d - \boldsymbol{p}^T (\boldsymbol{Q}\boldsymbol{u} - \boldsymbol{f}), \tag{27}$$

where

$$\boldsymbol{p} = [\lambda^0 \,|\, \pi_1^0 \,\pi_2^0 \,\pi_3^0 \,\pi_4^0 \,|\, \lambda^1 \,|\, \pi_1^1 \,\pi_2^1 \,\pi_3^1 \,\pi_4^1 \,|\, \lambda^2 \,|\, \cdots \,\pi_1^{N-1} \,\pi_2^{N-1} \,\pi_3^{N-1} \,\pi_3^{N-1} \,\pi_4^{N-1} \,|\, \lambda^N]^T, \tag{28}$$

$$\pi_k^i = \pi_k, \ \text{at } t = i\,\tau, k = 1, 2, 3, 4, \tag{29}$$

$$\lambda = [\lambda_h \,\lambda_u \,\lambda_v]^T, \tag{30}$$

$$\lambda^i = \lambda, \ \text{at } t = i\,\tau. \tag{31}$$

λ_h is the vector of nodal displacement-history-like adjoint variables. λ_u and λ_v are the vectors of nodal displacement-like and velocity-like adjoint variables, respectively. The first-order optimality conditions can now be obtained by taking derivatives of $\mathcal{A}$ with respect to $\boldsymbol{u}, \boldsymbol{p}$, and source parameters ξ or η.

4.2. State problem

Differentiating $\mathcal{A}$ with respect to $\boldsymbol{p}$ results in

$$\frac{\partial \mathcal{A}}{\partial \boldsymbol{p}} = \boldsymbol{0} \implies \boldsymbol{Q}\boldsymbol{u} = \boldsymbol{f}, \tag{32}$$

which is the same as the forward problem given by Equation (19).

4.3. Adjoint problem

Similarly, differentiating $\mathcal{A}$ with respect to $\mathbf{u}$ yields

$$\frac{\partial \mathcal{A}}{\partial \boldsymbol{u}} = \mathbf{0} \implies \boldsymbol{Q}^T \boldsymbol{p} = \frac{-2\boldsymbol{B}_{\dot{u}_a}\boldsymbol{u}}{(\boldsymbol{u}^T \boldsymbol{B}_{\dot{u}_a}\boldsymbol{u})^2}. \tag{33}$$

Equation (33) represents the *adjoint* problem associated with the inverse problem of interest. Because the adjoint problem involves $\boldsymbol{Q}^T$, we solve it by marching backwards in time. The adjoint force vector at any timestep i is given by

$$\mathbf{g}^i \equiv \frac{-2\mathbf{B}_{\dot{u}_a}\boldsymbol{u}}{(\boldsymbol{u}^T \mathbf{B}_{\dot{u}_a}\boldsymbol{u})^2} = \frac{-2\dot{\tilde{\mathbf{u}}}_a^i}{(\boldsymbol{u}^T \mathbf{B}_{\dot{u}_a}\boldsymbol{u})^2} = -2\mathcal{L}_d^2\,\dot{\tilde{\mathbf{u}}}_a^i. \tag{34}$$

Thus, the adjoint force vector at any timestep is obtained by scaling the vector of nodal velocity values in the target inclusion. The backward time marching is initiated at the final timestep ($i = N$), for which we obtain

$$\boldsymbol{\lambda}^N = \mathbf{g}^N. \tag{35}$$

We continue the time marching for $i = N-1, N-2, \ldots, 0$, by computing

$$\boldsymbol{\pi}_4^i = \frac{\tau}{6}\boldsymbol{\lambda}^{i+1}, \tag{36a}$$

$$\boldsymbol{\pi}_3^i = \frac{\tau}{3}\boldsymbol{\lambda}^{i+1} + \tau \mathbf{L}^T \boldsymbol{\pi}_4^i, \tag{36b}$$

$$\boldsymbol{\pi}_2^i = \frac{\tau}{3}\boldsymbol{\lambda}^{i+1} + \frac{\tau}{2}\mathbf{L}^T \boldsymbol{\pi}_3^i, \tag{36c}$$

$$\boldsymbol{\pi}_1^i = \frac{\tau}{6}\boldsymbol{\lambda}^{i+1} + \frac{\tau}{2}\mathbf{L}^T \boldsymbol{\pi}_2^i, \tag{36d}$$

$$\boldsymbol{\lambda}^i = \boldsymbol{\lambda}^{i+1} + \mathbf{L}^T(\boldsymbol{\pi}_1^i + \boldsymbol{\pi}_2^i + \boldsymbol{\pi}_3^i + \boldsymbol{\pi}_4^i) + \mathbf{g}^i, \tag{36e}$$

at each timestep, and updating $i \leftarrow (i-1)$ after each iteration.

4.4. Control problems

4.4.1. Time-signal optimization.
We define a vector of temporal nodal force parameters as

$$\boldsymbol{\xi} = [\xi_{11}\,\xi_{12}\ldots\xi_{1n_f}\ldots\xi_{n_s(n_f-1)}\,\xi_{n_s n_f}]^T. \tag{37}$$

During the inversion process, each element of this vector (ξ_{mn}) is updated using the derivative of the augmented functional with respect to ξ_{mn}, given by

$$\frac{\partial \mathcal{A}}{\partial \xi_{mn}} = \boldsymbol{p}^T \frac{\partial \boldsymbol{f}}{\partial \xi_{mn}} = \boldsymbol{\lambda}^0 \cdot \mathbf{y}_0 + \sum_{i=0}^{N-1}\left[\boldsymbol{\pi}_1^i \cdot \frac{\partial \mathbf{R}^i}{\partial \xi_{mn}} + \boldsymbol{\pi}_2^i \cdot \frac{\partial \mathbf{R}^{i+\frac{1}{2}}}{\partial \xi_{mn}} + \boldsymbol{\pi}_3^i \cdot \frac{\partial \mathbf{R}^{i+\frac{1}{2}}}{\partial \xi_{mn}} + \boldsymbol{\pi}_4^i \cdot \frac{\partial \mathbf{R}^{i+1}}{\partial \xi_{mn}}\right]$$
$$= \boldsymbol{\lambda}^0 \cdot \mathbf{y}_0 + \sum_{i=0}^{N-1}\left[\phi_n(i\tau)\boldsymbol{\pi}_1^i + \phi_n(i\tau + \frac{\tau}{2})[\boldsymbol{\pi}_2^i + \boldsymbol{\pi}_3^{i+1}] + \phi_n(i\tau + \tau)\boldsymbol{\pi}_4^i\right] \cdot \mathbf{R}_{sp}^m \tag{38}$$

$\mathbf{R}_{sp}^m$ is the spatial component of the force vector for the m-th source. The definition of $\mathbf{R}_{sp}^m$ and the details of the derivation of the gradient ($\frac{\partial \mathcal{A}}{\partial \xi_{mn}}$) are given in Appendix B.

Table II. Material and geometric properties for the layers and the inclusion shown in the geological formation model (Figure 2(a)).

Layer tag	Equations defining boundaries of the layers and the inclusion (all dimensions in meters)	Wave velocities C_p (m/s)	C_s (m/s)	Mass density (kg/m^3)
L1	$0 > x_3 > 2\arctan(\frac{x_1-3}{2}) - 18$	1005	615	2200
L2	$2\arctan(\frac{x_1-3}{2}) - 18 > x_3$	1199	734	2200
T	$(\frac{x_1}{3})^2 + (\frac{x_2}{3})^2 + (\frac{x_3+32.25}{3})^2 < 1$	389	238	2200

4.4.2. Load location optimization. The vector of load location parameters is given by

$$\boldsymbol{\eta} = [\eta_{11}\ \eta_{12} \ldots \eta_{n_s 1}\ \eta_{n_s 2}]^T. \tag{39}$$

The derivative of the augmented functional with respect to a load location parameter η_{mn} is given by

$$\frac{\partial \mathcal{A}}{\eta_{mn}} = \boldsymbol{p}^T \frac{\partial \boldsymbol{f}}{\partial \eta_{mn}} = \boldsymbol{\lambda}^0 \cdot \mathbf{y}_0 + \sum_{i=0}^{N-1} \left[\boldsymbol{\pi}_1^i \cdot \frac{\partial \mathbf{R}^i}{\partial \eta_{mn}} + \boldsymbol{\pi}_2^i \cdot \frac{\partial \mathbf{R}^{i+\frac{1}{2}}}{\partial \eta_{mn}} + \boldsymbol{\pi}_3^i \cdot \frac{\partial \mathbf{R}^{i+\frac{1}{2}}}{\partial \eta_{mn}} + \boldsymbol{\pi}_4^i \cdot \frac{\partial \mathbf{R}^{i+1}}{\partial \eta_{mn}} \right],$$

$$= \boldsymbol{\lambda}^0 \cdot \mathbf{y}_0 + \sum_{i=0}^{N-1} \left[f_m(i\tau)\boldsymbol{\pi}_1^i + f_m(i\tau + \frac{\tau}{2})[\boldsymbol{\pi}_2^i + \boldsymbol{\pi}_3^i] + f_m(i\tau + \tau)\boldsymbol{\pi}_4^i \right] \cdot \tilde{\mathbf{R}}_{\text{sp}}^m, \tag{40}$$

where $\tilde{\mathbf{R}}_{\text{sp}}^m$ is defined in Appendix B.

4.5. Summary of the inversion process

A summary of the inversion algorithm is given in Karve and Kallivokas (Table 2, [42]). We initialize the algorithm with a guess of the source time signals and the source locations. We, then, solve the state (forward) problem to obtain the velocity field within the target inclusion ($\dot{\tilde{u}}_a^i$) and compute the objective functional ($\mathcal{L}_d$) as well as the adjoint force vectors ($\mathbf{g}^i$). We use the adjoint force vectors to resolve the adjoint problem and obtain the values of the adjoint variables ($\boldsymbol{\pi}_j^i$) on Γ_{load}. We, then, compute the gradient(s) of the augmented functional using Equations (38) and (40) and obtain the search direction(s) using the conjugate gradient method. We use scalar step lengths (α_t and/or α_l) to obtain $\boldsymbol{\xi}$ and/or $\boldsymbol{\eta}$ for the next inversion iteration and repeat the process until convergence.

5. NUMERICAL EXPERIMENTS

We test the inverse source algorithm by performing numerical experiments on a synthetically created geological formation model (Figure 2(a)). The formation model contains two layers (L1 and L2) and a target inclusion (T). The material properties of the layers and the equations defining the geometries of the inter-layer boundaries are given in Table II. The target inclusion (T) is spherical in shape, and its diameter is 6 m. The centroid of the target inclusion is located 32.25 m below the ground surface ($x_3 = 0$). In order to reduce the computational effort required to resolve the inverse source problem, we select a subset of the geo-formation shown in Figure 2(a) as our computational domain. The dimensions of the selected computational domain are 24 m × 24 m × 39m. We use 7.5-m-thick PML zones at the truncation boundaries of the computational domain to mimic the semi-infinite nature of the domain of interest. The computational domain and the PMLs are shown in Figure 2(b). We discretize the computational domain using a structured mesh of 27-noded, regular hexahedral, spectral elements of size 0.75 m × 0.75 m × 0.75 m. We employ the 4th-order Runge–Kutta method (discussed in Section 2.4), with timestep $\tau = 0.00025$s, for time integration, and simulate the wave propagation in the computational domain for a total time of 0.6s (i.e., $T = 0.6$ s).

(a) Geological formation model

(b) The computational domain

(c) A section through the $x_1 - x_3$ plane

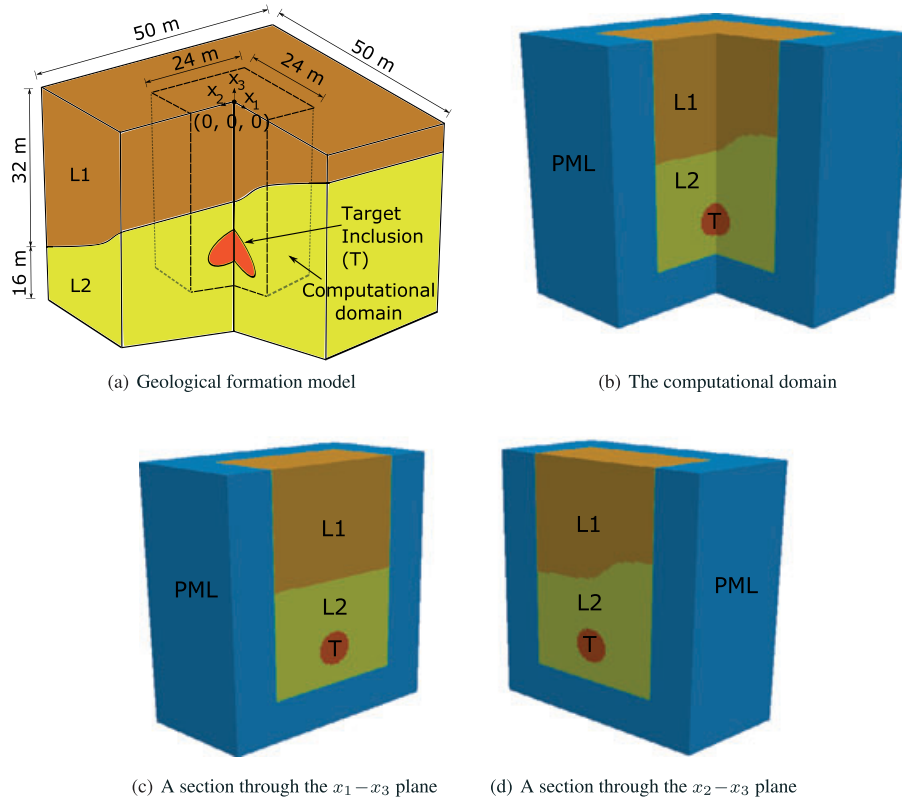(d) A section through the $x_2 - x_3$ plane

Figure 2. Geological formation model and computational domain (material properties and geometric description are given in Table II). [Colour figure can be viewed at wileyonlinelibrary.com]

In order to compare the performance of various spatio-temporal source characteristics, we define the following motion metrics. If $\dot{\mathbf{u}}^i$ is the vector of the x_1-directional, x_2-directional, and x_3-directional velocity components at a computational node at time $t = i\tau$, then we define the time-averaged kinetic energy at that node as

$$\text{KE}_{\text{TA}} = \frac{1}{2}\rho \left[\frac{\tau}{2} \dot{\mathbf{u}}^0 \cdot \dot{\mathbf{u}}^0 + \frac{\tau}{2} \dot{\mathbf{u}}^N \cdot \dot{\mathbf{u}}^N + \tau \sum_{i=1}^{N-1} \dot{\mathbf{u}}^i \cdot \dot{\mathbf{u}}^i \right] \Big/ T, \tag{41}$$

where ρ is the mass density. Furthermore, we define the time-averaged kinetic energy of the target inclusion as

$$\text{KE}_{\text{inc}} = \frac{1}{2} \left[\frac{\tau}{2} (\dot{\tilde{\mathbf{u}}}_a^0 \cdot \mathbf{M}_{\text{inc}} \dot{\tilde{\mathbf{u}}}_a^0 + \dot{\tilde{\mathbf{u}}}_a^N \cdot \mathbf{M}_{\text{inc}} \dot{\tilde{\mathbf{u}}}_a^N) + \tau \sum_{i=1}^{N-1} \dot{\tilde{\mathbf{u}}}_a^i \cdot \mathbf{M}_{\text{inc}} \dot{\tilde{\mathbf{u}}}_a^i \right] \Big/ T, \tag{42}$$

where $\tilde{\mathbf{u}}_a^i$ is defined in Equation (12) and $\mathbf{M}_{\text{inc}}$ is the mass matrix for the target inclusion. We remark that the time-averaged kinetic energy definitions (Equations (41) and (42)) are the spatio-temporally discretized versions of the continuous definitions given by

$$\text{KE}_{\text{TA}}^c = \int_0^T \frac{1}{2}\rho \left[\dot{\mathbf{u}}(t) \cdot \dot{\mathbf{u}}(t) \right] dt \Big/ T, \tag{43}$$

$$\text{KE}_{\text{inc}}^c = \int_{\Omega_a} \int_0^T \frac{1}{2}\rho_a \left[\dot{\mathbf{u}}_a(t) \cdot \dot{\mathbf{u}}_a(t) \right] dt \, d\Omega \Big/ T, \tag{44}$$

where $\dot{\mathbf{u}}(t)$ is the vector containing the x_1-directional, x_2-directional, and x_3-directional components of velocity at a computational node and $\dot{\mathbf{u}}_a(t)$ is the velocity vector for a computational node within the target inclusion. The units of KE_{TA} are J/m^3 and those of KE_{inc} are J. In our numerical experiments, we use plots of KE_{TA} and values of KE_{inc} to assess the degree of energy focusing. Next, we describe the numerical experiments and discuss their results.

5.1. Experiment 1 – frequency sweeps and source polarization effect

In this experiment, we use the frequency sweep approach to determine the source frequencies that could produce a strong wave energy focusing at the target. Accordingly, we apply a uniform (horizontally or vertically polarized) load of magnitude 50 kN/m^2 on the free surface ($x_3 = 0$) of the computational domain. We compute the objective functional ($\mathcal{L}_d$) and the time-averaged kinetic energy of the target inclusion (KE_{inc}) for a range of source frequencies driving the uniform load. The results are shown in Figure 3: it can be seen that for a uniform horizontal load, the minimum value of $\mathcal{L}_d$ and the maximum value of KE_{inc} occur at a source frequency of, approximately, 72 Hz. Thus, the frequency sweep enables determination of the *amplification frequencies* of the target formation. In a field implementation of the wave-based EOR, if the locations of the finite-width sources are chosen arbitrarily, or decided solely based on practical considerations, then one could use the
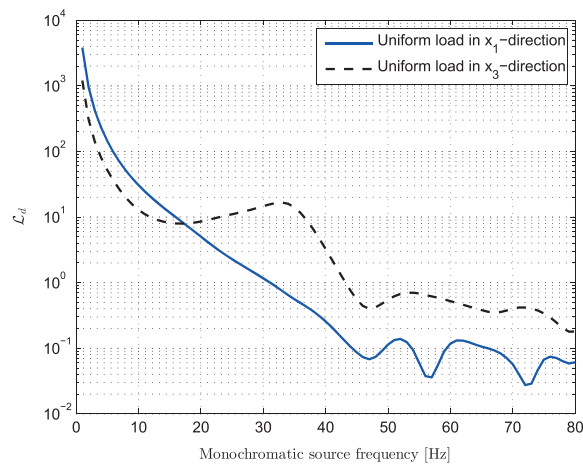
(a) Motion metric $\mathcal{L}_d$ of the target inclusion
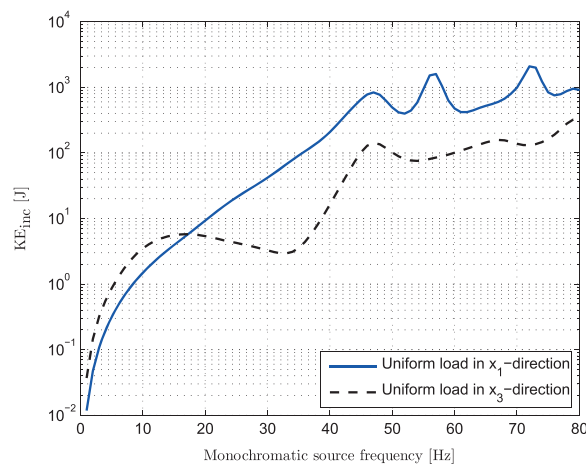
(b) Time-averaged kinetic energy of the target inclusion

Figure 3. Frequency sweep for horizontal and vertical loads. [Colour figure can be viewed at wileyonlinelibrary.com]

Table III. The initial guess of source locations.

Load number (i)	η_{i1} (m)	η_{i2} (m)
1	8.00	9.00
2	−9.00	7.00
3	−8.00	−7.00
4	8.00	−6.00

amplification frequency as the driving frequency for the sources. For example, if n_s horizontally polarized wave sources are to be applied on the free surface of the geo-formation in Figure 2(a), then one could use $f_i(t) = (50 \text{ kN/m}^2) \sin[2\pi(72)t]$ for $i = 1, 2, \ldots, n_s$.

The frequency sweep also gives insights into the effect of source polarization on the wave energy delivery to the target formation. In [46], Sánchez-Sesma *et al.* discussed the energy partitions for horizontal and vertical unit harmonic point loads acting on a homogeneous elastic halfspace. They reported that a vertical load radiates about 55% to 75% of the energy in the form of Rayleigh surface waves (depending on Poisson's ratio). A horizontal load, on the other hand, expends only about 10% to 30% of the wave energy in the form of Rayleigh waves. Thus, horizontally polarized loads seem to be more efficient at delivering the wave energy to deeply situated target formations. Figure 3(b) shows that the value of KE_{inc} for the horizontal loads is greater than that for the vertical loads for most of the driving frequencies considered in this experiment. Furthermore, the maximum value of KE_{inc} for the horizontal loads is about five times that for the vertical loads. This experiment indicates that the efficiency of the wave energy delivery can be increased by using horizontally polarized surface sources instead of vertically polarized sources.

We remark that in our analysis we did not consider the effect of material or intrinsic attenuation. Material attenuation can be included either by adopting models based on Q-factors, or by incorporating an attenuation model in the analysis (this will amount to modifying the damping matrix $\mathbf{C}$ in Equation (10)). The inverse source procedure can be used for computing the optimal spatio-temporal characteristics of horizontally, vertically, or obliquely polarized surface loads.

5.2. Experiment 2 – source time signal optimization

In this experiment, we compare the frequency sweep and the inverse source approaches for deciding the time signals driving the surface sources that maximize the wave energy delivery to the target inclusion. We use four, horizontally polarized surface loads (acting along the x_1 direction) to initiate the wave motion. The spatial variability of the surface sources is given by Equation (24). We set $b_{i1} = b_{i2} = 1.25$ m, and the locations of the centerlines of the loads (η_{i1} and η_{i2}) are given in Table III.

For the frequency sweep approach, we consult Figure 3 and decide to employ monochromatic source signals with a dominant frequency of 72Hz. Thus, we set $f_i(t) = (50 \text{ kN/m}^2) \sin[2\pi(72)t]$ for $i = 1, 2, \ldots, 4$. When surface loads, described by the $f_i(t)$ and (η_{i1}, η_{i2}) locations given in Table III, are used to excite the wave motion in the computational domain, the value of KE_{inc} is about 0.73 J. Of interest is how the time signals computed using the inverse source approach compare in terms of the energy delivery to the target inclusion, against the monochromatic signals suggested by the frequency sweep. To this end, we start with an initial guess of the time signals, which is shown in Figure 4. Figure 4 shows that the spectrum of the initial guess contains a wide range of frequencies.

We, then, use the procedure outlined in Section 4.5 to maximize the wave energy delivery to the target formation by seeking the optimal time signals for the sources while keeping their locations fixed. The maximum amplitude of the loads is restricted to 50 kN/m². The converged time signals and their frequency spectra are shown in Figure 5. The resulting distribution of the time-averaged kinetic energy in the computational domain is shown in Figure 7(a). It can be seen in Figure 5(b) that the converged signals have two dominant frequencies, approximately, 56 Hz and 72 Hz. The time-averaged kinetic energy (KE_{inc}) for the converged signals is 0.88 J. The fact that one of the dominant
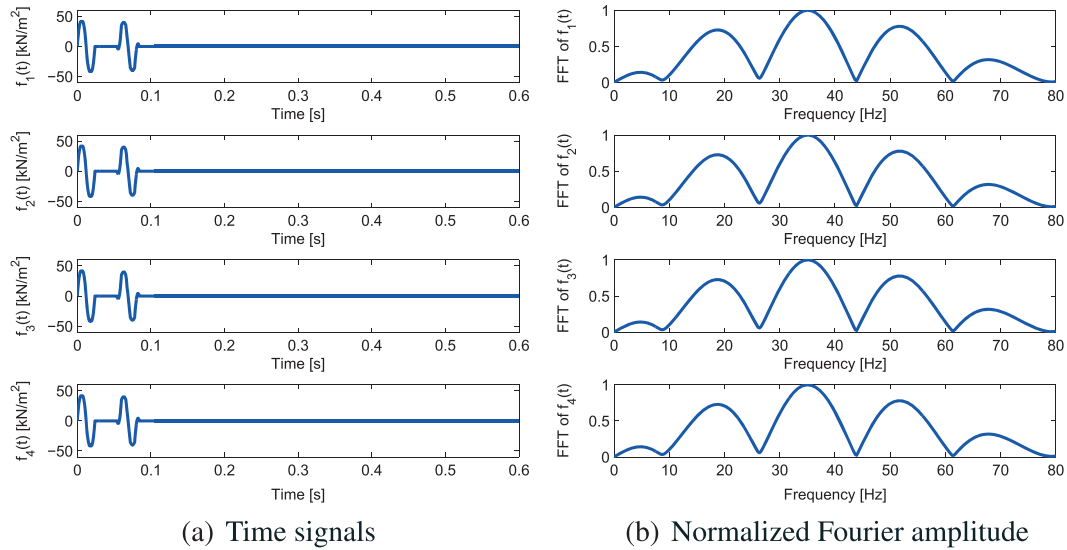
(a) Time signals   (b) Normalized Fourier amplitude

Figure 4. Initial guess of source time signals and the associated frequency spectra. [Colour figure can be viewed at wileyonlinelibrary.com]

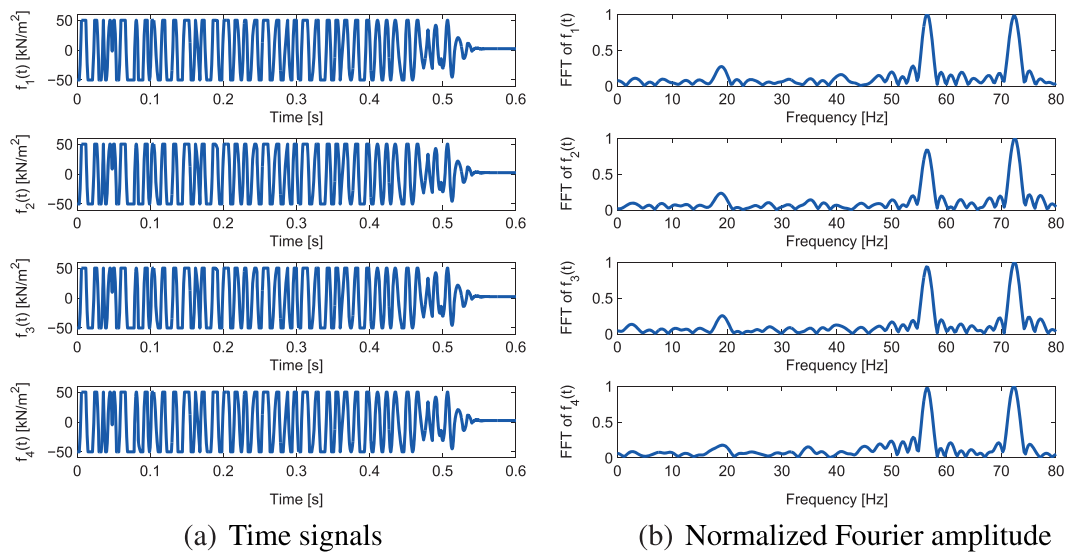(a) Time signals   (b) Normalized Fourier amplitude

Figure 5. Converged time signals and the associated frequency spectra after time signal optimization. [Colour figure can be viewed at wileyonlinelibrary.com]

frequencies of the converged signals (72 Hz) is equal to the amplification frequency suggested by the frequency sweep is a validation of the inverse source approach.

This experiment highlights the key differences between the frequency sweep and the inverse source approaches. For the geostructure considered in this experiment, the optimal time signals suggested by the inverse source procedure were able to deliver about 20% more time-averaged kinetic energy to the target than that delivered by the best monochromatic signals selected using the frequency sweep method. We remark that a frequency sweep conducted using a uniform load applied on the entire surface of the computational domain can become blind to the complex interference patterns generated by the waves emitted by finite-width sources. To alleviate this drawback, a frequency sweep can be conducted using a number of finite-width sources. We remark that a combined frequency-and-location sweep becomes computationally prohibitive.

Table IV. Converged source locations after the source location optimization.

Load number (i)	η_{i1} (m)	η_{i2} (m)
1	−1.21	−0.03
2	−1.06	0.28
3	−0.88	0.15
4	−0.25	0.05

5.3. Experiment 3 – source location optimization

In this experiment, we discuss computation of the optimal source locations while keeping the source time signals fixed. The source time signals can be chosen using the frequency sweep approach, the time-reversal approach, or the inverse source approach. Here, we illustrate the procedure using the optimal time signals obtained in experiment 2. The initial guess of the source locations is given in Table III and the (fixed) time signals are shown in Figure 5. We, now, seek the optimal source locations using the inverse source algorithm described in Section 4.5. The converged source locations are given in Table IV, and the plot of time-averaged kinetic energy after the source location optimization is shown in Figure 7(b). The time-averaged kinetic energy of the inclusion (KE_{inc}) after the source location optimization is 1.68 J.

The results of this numerical experiment highlight the importance of source location optimization. The KE_{inc} value after time signal optimization was 0.88 J. Placing the loads at the optimal locations resulted in a 90% increase in the value of KE_{inc} (0.88 to 1.68 J). In a field implementation of the wave-based EOR, the stress wave stimulation will be applied for days. Thus, a 90% increase in the energy delivery could result in significant improvement in the efficiency of the sought mobilization process.

5.4. Experiment 4 – simultaneous optimization of spatio-temporal source characteristics

The simultaneous optimization process is initialized with a guess of source time signals and source locations. Both temporal and spatial source characteristics are updated during each inversion iteration to arrive at the optimal spatio-temporal source characteristics. We illustrate the simultaneous optimization procedure in this numerical experiment. We start the inversion process with the initial guess of source time signals and source locations given in Figure 4 and Table III, respectively. We, then, use the inverse source algorithm summarized in Section 4.5 to obtain optimal spatio-temporal source characteristics. The converged source locations are given in Table V, while the converged time signals and the associated frequency spectra are shown in Figure 6. The plot of the time-averaged kinetic energy for the optimal time signals and load locations is shown in Figure 7(c). The converged source time signals and locations are similar to those obtained by the sequential time-signal-location optimization process (Figure 5 and Table IV). The time-averaged kinetic energy of the inclusion after the simultaneous spatio-temporal optimization is about 1.88 J (as opposed to 1.68 J for the sequential optimization), which is about two times the value achieved after source time signal optimization. Thus, once again, the results highlight the importance of source location optimization. We remark that the simultaneous optimization process provides more freedom for fine-tuning the spatio-temporal source characteristics, and hence, it may perform better than the sequential optimization process, especially for geostructures exhibiting a high degree of heterogeneity.

5.5. Experiment 5 – uncertainty effects of the geostructure's material properties

In the preceding sections, our inverse source formulation and numerical experimentation assumed a priori knowledge about the material properties of the geostructure of interest. In practice,

(a) Time signals   (b) Normalized Fourier amplitude
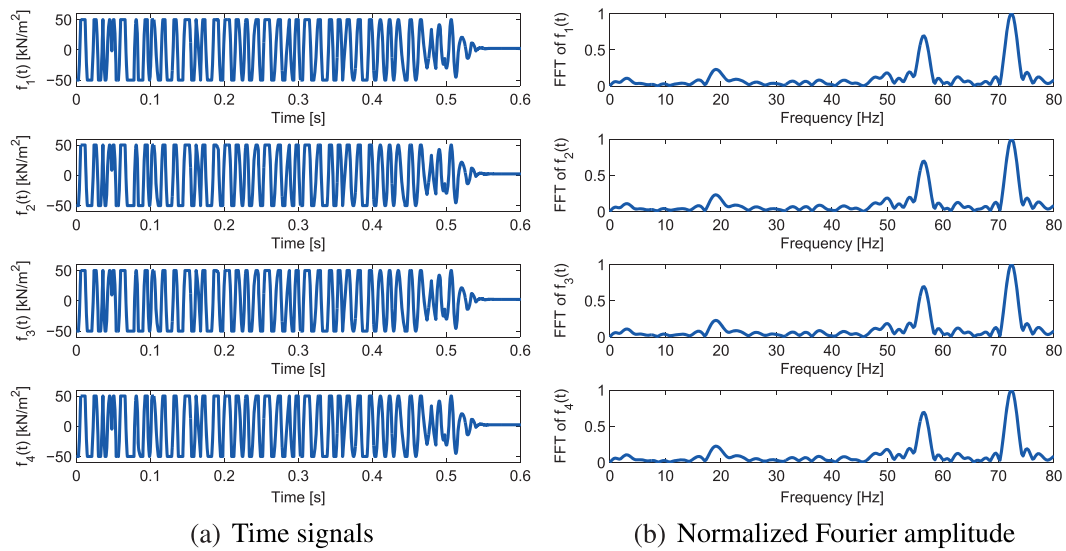
Figure 6. Converged time signals and the associated frequency spectra after simultaneous optimization. [Colour figure can be viewed at wileyonlinelibrary.com]

(a) $\mathrm{KE_{TA}}$ after source time signal optimization, $\mathrm{KE_{inc}} = 0.88\mathrm{J}$ (Experiment 2)

(b) $\mathrm{KE_{TA}}$ after sequential source time signal and location optimization, $\mathrm{KE_{inc}} = 1.68\mathrm{J}$ (Experiment 3)

(c) $\mathrm{KE_{TA}}$ after simultaneous source time signal and location optimization, $\mathrm{KE_{inc}} = 1.88\mathrm{J}$ (Experiment 4)

Figure 7. The plots of time-averaged kinetic energy ($\mathrm{KE_{TA}}$). [Colour figure can be viewed at wileyonlinelibrary.com]

Table V. Converged source locations after
simultaneous optimization

Load number (i)	η_{i1} (m)	η_{i2} (m)
1	-0.81	-0.02
2	-0.88	-0.01
3	-0.76	-0.01
4	-0.83	0.04

Table VI. 'True' material properties for
the layers and the inclusion shown in the
geological formation model (Figure 2(a)).

| Layer tag | Wave velocities | |
	C_p (m/s)	C_s (m/s)
L1	926	567
L2	1066	652
T	438	268

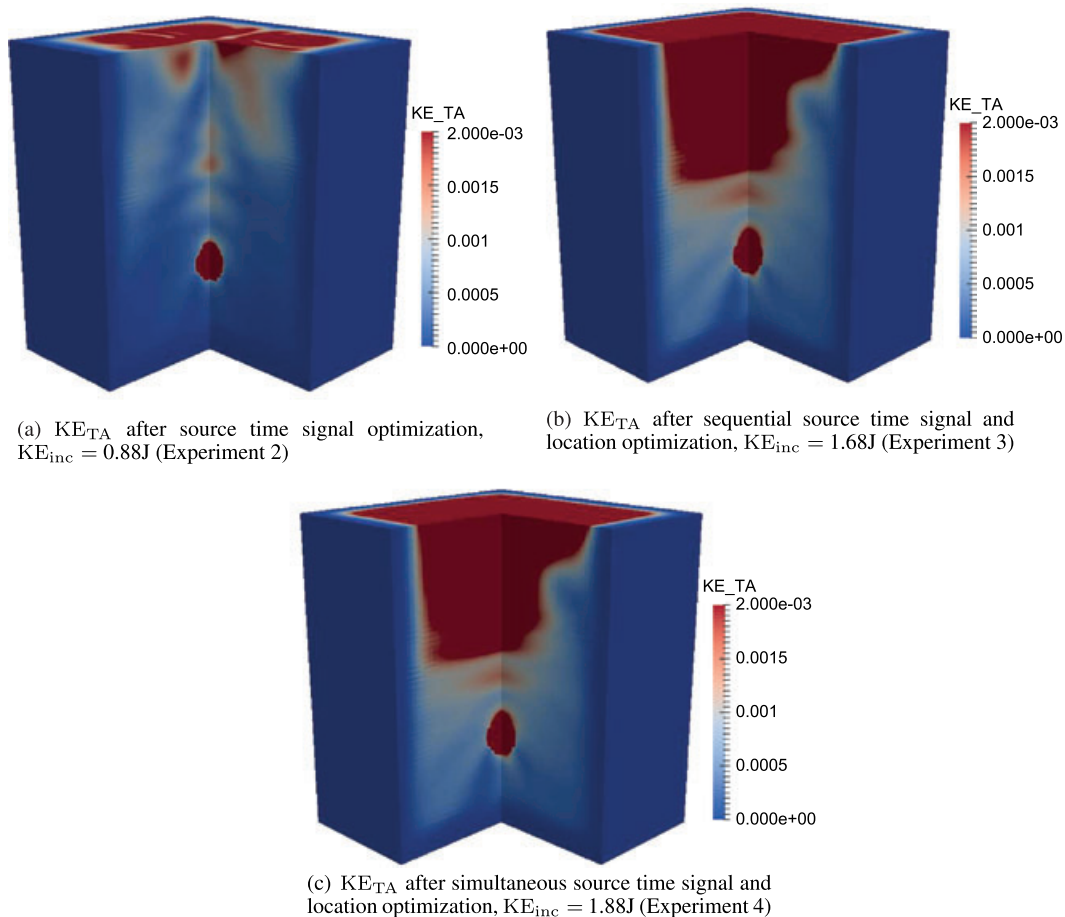however, the material properties of the layered formations and the target are not precisely known. We illustrate the effect of uncertainty in our knowledge of the material properties by conducting the following numerical test: we assume that the material properties used in our computational model are 'incorrect', and that the 'true' material properties are those given in Table VI, reflecting a change of 10% to 30% in the values of the Lamé parameters. We, then, use the wave sources endowed with the 'optimal' spatio-temporal characteristics computed using the 'incorrect' material properties (in experiment 4, i.e., Table V and Figure 6) to excite the wave motion in the computational domain endowed with the 'true' material properties. The resulting value of KE_{inc} was reduced from 1.88 J (experiment 4) to 0.78 J – a reduction of about 58%. Thus, the simple numerical test shows how imperfect knowledge of the material properties can adversely affect wave energy focusing. This observation calls for a formal treatment of the uncertainties in the input data – either by formulating and resolving a Bayesian inverse source problem or by quantifying the effects of uncertainties in the input using sensitivity and/or reliability analyses. In [47], Karve *et al.* discussed a systematic framework for evaluating the uncertainty in the wave energy delivery to targeted geo-formations. They formulated the wave propagation problem for a two-dimensional, elastic geostructure, and performed sensitivity as well as first-order reliability analyses to compute the probabilities of failure to achieve threshold values of KE_{inc}. In their work, the uncertainty in the knowledge of the material properties was modeled by assigning suitable probability distribution functions to the Lamé parameters. Similar analysis can be performed for a three-dimensional, elastic geostructure. We remark that the uncertainties in the knowledge of the material properties tend to reduce the amount of the kinetic energy delivered to the target, but the focusing appears to remain intact.

6. CONCLUSIONS

We discussed an inverse source approach for designing wave energy delivery systems used to apply stress wave stimulations to targeted subsurface formations. We provided evidence of the method's ability to resolve the optimal spatio-temporal characteristics that focus the wave energy to the targeted formation by conducting numerical experiments on a prototype geological formation. Our numerical experiments indicate that optimal load locations play a key role in delivering vibrational energy to the targeted formation and that horizontally polarized loads are preferred for delivering wave energy to deeply situated geological formations than vertically polarized loads. The inverse

source and the associated reliability quantification [47] methodologies provide an analytical framework for designing field implementations in applications of interest to wave-based enhanced oil recovery.

APPENDIX A: THE MATRIX Q

$$Q = \begin{bmatrix}
\mathbf{I} & \mathbf{0} & \mathbf{0} & \mathbf{0} & \mathbf{0} & \mathbf{0} & \mathbf{0} & \mathbf{0} & \mathbf{0} & \mathbf{0} & \cdots & \mathbf{0} & \mathbf{0} & \mathbf{0} & \mathbf{0} & \mathbf{0} & \mathbf{0} \\
-\mathbf{L} & \mathbf{I} & \mathbf{0} & \mathbf{0} & \mathbf{0} & \mathbf{0} & \mathbf{0} & \mathbf{0} & \mathbf{0} & \mathbf{0} & \cdots & \mathbf{0} & \mathbf{0} & \mathbf{0} & \mathbf{0} & \mathbf{0} & \mathbf{0} \\
-\mathbf{L} & \frac{-\tau}{2}\mathbf{L} & \mathbf{I} & \mathbf{0} & \mathbf{0} & \mathbf{0} & \mathbf{0} & \mathbf{0} & \mathbf{0} & \mathbf{0} & \cdots & \mathbf{0} & \mathbf{0} & \mathbf{0} & \mathbf{0} & \mathbf{0} & \mathbf{0} \\
-\mathbf{L} & \mathbf{0} & \frac{-\tau}{2}\mathbf{L} & \mathbf{I} & \mathbf{0} & \mathbf{0} & \mathbf{0} & \mathbf{0} & \mathbf{0} & \mathbf{0} & \cdots & \mathbf{0} & \mathbf{0} & \mathbf{0} & \mathbf{0} & \mathbf{0} & \mathbf{0} \\
-\mathbf{L} & \mathbf{0} & \mathbf{0} & -\tau\mathbf{L} & \mathbf{I} & \mathbf{0} & \mathbf{0} & \mathbf{0} & \mathbf{0} & \mathbf{0} & \cdots & \mathbf{0} & \mathbf{0} & \mathbf{0} & \mathbf{0} & \mathbf{0} & \mathbf{0} \\
-\mathbf{I} & \frac{-\tau}{6}\mathbf{I} & \frac{-\tau}{3}\mathbf{I} & \frac{-\tau}{3}\mathbf{I} & \frac{-\tau}{6}\mathbf{I} & \mathbf{I} & \mathbf{0} & \mathbf{0} & \mathbf{0} & \mathbf{0} & \cdots & \mathbf{0} & \mathbf{0} & \mathbf{0} & \mathbf{0} & \mathbf{0} & \mathbf{0} \\
\mathbf{0} & \mathbf{0} & \mathbf{0} & \mathbf{0} & \mathbf{0} & -\mathbf{L} & \mathbf{I} & \mathbf{0} & \mathbf{0} & \mathbf{0} & \cdots & \mathbf{0} & \mathbf{0} & \mathbf{0} & \mathbf{0} & \mathbf{0} & \mathbf{0} \\
\mathbf{0} & \mathbf{0} & \mathbf{0} & \mathbf{0} & \mathbf{0} & -\mathbf{L} & \frac{-\tau}{2}\mathbf{L} & \mathbf{I} & \mathbf{0} & \mathbf{0} & \cdots & \mathbf{0} & \mathbf{0} & \mathbf{0} & \mathbf{0} & \mathbf{0} & \mathbf{0} \\
\mathbf{0} & \mathbf{0} & \mathbf{0} & \mathbf{0} & \mathbf{0} & -\mathbf{L} & \mathbf{0} & \frac{-\tau}{2}\mathbf{L} & \mathbf{I} & \mathbf{0} & \cdots & \mathbf{0} & \mathbf{0} & \mathbf{0} & \mathbf{0} & \mathbf{0} & \mathbf{0} \\
\mathbf{0} & \mathbf{0} & \mathbf{0} & \mathbf{0} & \mathbf{0} & -\mathbf{L} & \mathbf{0} & \mathbf{0} & -\tau\mathbf{L} & \mathbf{I} & \cdots & \mathbf{0} & \mathbf{0} & \mathbf{0} & \mathbf{0} & \mathbf{0} & \mathbf{0} \\
\mathbf{0} & \mathbf{0} & \mathbf{0} & \mathbf{0} & \mathbf{0} & -\mathbf{I} & \frac{-\tau}{6}\mathbf{I} & \frac{-\tau}{3}\mathbf{I} & \frac{-\tau}{3}\mathbf{I} & \frac{-\tau}{6}\mathbf{I} & \cdots & \mathbf{0} & \mathbf{0} & \mathbf{0} & \mathbf{0} & \mathbf{0} & \mathbf{0} \\
\mathbf{0} & \mathbf{0} & \mathbf{0} & \mathbf{0} & \mathbf{0} & \mathbf{0} & \mathbf{0} & \mathbf{0} & \mathbf{0} & \mathbf{0} & \cdots & \mathbf{0} & \mathbf{0} & \mathbf{0} & \mathbf{0} & \mathbf{0} & \mathbf{0} \\
\vdots & \vdots & \vdots & \vdots & \vdots & \vdots & \vdots & \vdots & \vdots & \vdots & \ddots & \vdots & \vdots & \vdots & \vdots & \vdots & \vdots \\
\mathbf{0} & \mathbf{0} & \mathbf{0} & \mathbf{0} & \mathbf{0} & \mathbf{0} & \mathbf{0} & \mathbf{0} & \mathbf{0} & \mathbf{0} & \cdots & \mathbf{0} & \mathbf{0} & \mathbf{0} & \mathbf{0} & \mathbf{0} & \mathbf{0} \\
\mathbf{0} & \mathbf{0} & \mathbf{0} & \mathbf{0} & \mathbf{0} & \mathbf{0} & \mathbf{0} & \mathbf{0} & \mathbf{0} & \mathbf{0} & \cdots & \mathbf{I} & \mathbf{0} & \mathbf{0} & \mathbf{0} & \mathbf{0} & \mathbf{0} \\
\mathbf{0} & \mathbf{0} & \mathbf{0} & \mathbf{0} & \mathbf{0} & \mathbf{0} & \mathbf{0} & \mathbf{0} & \mathbf{0} & \mathbf{0} & \cdots & -\mathbf{L} & \mathbf{I} & \mathbf{0} & \mathbf{0} & \mathbf{0} & \mathbf{0} \\
\mathbf{0} & \mathbf{0} & \mathbf{0} & \mathbf{0} & \mathbf{0} & \mathbf{0} & \mathbf{0} & \mathbf{0} & \mathbf{0} & \mathbf{0} & \cdots & -\mathbf{L} & \frac{-\tau}{2}\mathbf{L} & \mathbf{I} & \mathbf{0} & \mathbf{0} & \mathbf{0} \\
\mathbf{0} & \mathbf{0} & \mathbf{0} & \mathbf{0} & \mathbf{0} & \mathbf{0} & \mathbf{0} & \mathbf{0} & \mathbf{0} & \mathbf{0} & \cdots & -\mathbf{L} & \mathbf{0} & \frac{-\tau}{2}\mathbf{L} & \mathbf{I} & \mathbf{0} & \mathbf{0} \\
\mathbf{0} & \mathbf{0} & \mathbf{0} & \mathbf{0} & \mathbf{0} & \mathbf{0} & \mathbf{0} & \mathbf{0} & \mathbf{0} & \mathbf{0} & \cdots & -\mathbf{L} & \mathbf{0} & \mathbf{0} & -\tau\mathbf{L} & \mathbf{I} & \mathbf{0} \\
\mathbf{0} & \mathbf{0} & \mathbf{0} & \mathbf{0} & \mathbf{0} & \mathbf{0} & \mathbf{0} & \mathbf{0} & \mathbf{0} & \mathbf{0} & \cdots & -\mathbf{I} & \frac{-\tau}{6}\mathbf{I} & \frac{-\tau}{3}\mathbf{I} & \frac{-\tau}{3}\mathbf{I} & \frac{-\tau}{6}\mathbf{I} & \mathbf{I}
\end{bmatrix}, \tag{A.1}$$

where the matrix $\mathbf{L}$ is defined in Equation (16b), $\mathbf{I}$ is the identity matrix, and τ is the timestep.

APPENDIX B: CONTROL PROBLEMS

We recall that the vector $\mathbf{R}$ at the k-th timestep is defined as

$$\mathbf{R}^k = \mathbf{M}^{-1} \begin{bmatrix} \mathbf{0} \\ \mathbf{0} \\ \mathbf{F}^k \end{bmatrix} = \mathbf{M}^{-1} \begin{bmatrix} \mathbf{0} \\ \mathbf{0} \\ \sum_{j=1}^{n_s} \mathbf{F}_{sp}^j \cdot f_j(k\tau) \end{bmatrix}, \tag{B.1}$$

where $\mathbf{F}_{sp}^j$ is the vector of nodal values corresponding to the spatial variation of the j-th source and the function $f_j(t)$ defines the value of j-th source at time t. We remark that $\mathbf{F}_{sp}^j$ is assembled using element force vectors for the j-th load, given by

$$\mathbf{F}_{elem}^j = \begin{bmatrix} \mathbf{F}_{elem,x_1}^j \\ \mathbf{F}_{elem,x_2}^j \\ \mathbf{F}_{elem,x_3}^j \end{bmatrix} = \int_{\Gamma_{elem}^{load}} \begin{bmatrix} \boldsymbol{\theta}_{j1}(\mathbf{x}, \eta_{j1}, \eta_{j2})\boldsymbol{\Phi}\delta_{1p} \\ \boldsymbol{\theta}_{j2}(\mathbf{x}, \eta_{j1}, \eta_{j2})\boldsymbol{\Phi}\delta_{2p} \\ \boldsymbol{\theta}_{j3}(\mathbf{x}, \eta_{j1}, \eta_{j2})\boldsymbol{\Phi}\delta_{3p} \end{bmatrix} d\Gamma, \tag{B.2}$$

where δ_{lp} ($l = 1, 2, 3$) is the Kronecker delta, $\Gamma_{\text{elem}}^{\text{load}}$ is the loaded boundary for the element, and x_p is the loading direction. We use Equations (B.1) and (B.2) to compute the derivatives of $\mathbf{R}^k$ with respect to temporal parameters ξ_{mn} and location parameters η_{mn}.

B.1. Time signal optimization

The control equation for time signal optimization (Equation 38) involves the derivative of $\mathbf{R}^k$ with respect to ξ_{mn}, or

$$\frac{\partial \mathbf{R}^k}{\partial \xi_{mn}} = \mathbf{M}^{-1} \begin{bmatrix} \mathbf{0} \\ \mathbf{0} \\ \mathbf{F}_{sp}^m \left(\frac{\partial f_m(k\tau)}{\partial \xi_{mn}} \right) \end{bmatrix} = \mathbf{M}^{-1} \begin{bmatrix} \mathbf{0} \\ \mathbf{0} \\ \mathbf{F}_{\text{sp}}^m \end{bmatrix} \phi_n(k\tau). \tag{B.3}$$

Thus, we update each element (ξ_{mn}) of the control parameter vector $\boldsymbol{\xi}$, using

$$\frac{\partial \mathcal{A}}{\partial \xi_{mn}} = \boldsymbol{\lambda}^0 \cdot \mathbf{y}_0 + \sum_{i=0}^{N-1} \left[\phi_n(i\tau)\boldsymbol{\pi}_1^i + \phi_n(i\tau + \frac{\tau}{2})[\boldsymbol{\pi}_2^i + \boldsymbol{\pi}_3^i] + \phi_n(i\tau + \tau)\boldsymbol{\pi}_4^i \right] \cdot \mathbf{R}_{\text{sp}}^m, \tag{B.4}$$

where

$$\mathbf{R}_{\text{sp}}^m = \mathbf{M}^{-1} \begin{bmatrix} \mathbf{0} \\ \mathbf{0} \\ \mathbf{F}_{\text{sp}}^m \end{bmatrix}. \tag{B.5}$$

B.2. Load location optimization

The derivative of $\mathbf{R}^k$ with respect a location parameter (η_{mn}) is given as

$$\frac{\partial \mathbf{R}^k}{\partial \eta_{mn}} = \mathbf{M}^{-1} \begin{bmatrix} \mathbf{0} \\ \mathbf{0} \\ \frac{\partial \mathbf{F}_{sp}^m}{\partial \eta_{mn}} f_m(k\tau) \end{bmatrix} = \mathbf{M}^{-1} \begin{bmatrix} \mathbf{0} \\ \mathbf{0} \\ \tilde{\mathbf{F}}_{\text{sp}}^m \end{bmatrix} f_m(k\tau), \tag{B.6}$$

where $\tilde{\mathbf{F}}_{\text{sp}}^m$ is assembled using derivatives of element force vectors for m-th load, given by

$$\frac{\partial \mathbf{F}_{\text{elem}}^m}{\partial \eta_{mn}} = \int_{\Gamma_{\text{elem}}^{\text{load}}} \begin{bmatrix} \frac{\partial \boldsymbol{\theta}_{m1}(\mathbf{x}, \eta_{m1}, \eta_{m2})}{\partial \eta_{mn}} \boldsymbol{\Phi} \delta_{1p} \\ \frac{\partial \boldsymbol{\theta}_{m2}(\mathbf{x}, \eta_{m1}, \eta_{m2})}{\partial \eta_{mn}} \boldsymbol{\Phi} \delta_{2p} \\ \frac{\partial \boldsymbol{\theta}_{m3}(\mathbf{x}, \eta_{m1}, \eta_{m2})}{\partial \eta_{mn}} \boldsymbol{\Phi} \delta_{3p} \end{bmatrix} d\Gamma. \tag{B.7}$$

Thus, we update each element (η_{mn}) of the control parameter vector $\boldsymbol{\eta}$, using

$$\frac{\partial \mathcal{A}}{\eta_{mn}} = \boldsymbol{\lambda}^0 \cdot \mathbf{y}_0 + \sum_{i=0}^{N-1} \left[f_m(i\tau)\boldsymbol{\pi}_1^i + f_m(i\tau + \frac{\tau}{2})[\boldsymbol{\pi}_2^i + \boldsymbol{\pi}_3^i] + f_m(i\tau + \tau)\boldsymbol{\pi}_4^i \right] \cdot \tilde{\mathbf{R}}_{\text{sp}}^m, \tag{B.8}$$

where

$$\tilde{\mathbf{R}}_{\text{sp}}^m = \mathbf{M}^{-1} \begin{bmatrix} \mathbf{0} \\ \mathbf{0} \\ \tilde{\mathbf{F}}_{\text{sp}}^m \end{bmatrix}. \tag{B.9}$$

REFERENCES

1. Lake LW. *Enhanced Oil Recovery*. Society of Petroleum Engineers, 2010.
2. Steinbrugge KV, Moran DF. An engineering study of the Southern California earthquake of July 21, 1952 and its aftershocks. *Bulletin of the Seismological Society of America* 1954; **44**(2B):201–462.
3. Smimova MN. Effect of eartquakes on the yield of Gudermes field (Northeastern Caucasus). *Fizika Zemli (Physics of the Solid Earth)* 1968; **12**:71–75.

4. Voytov GI, Osika GD, Plotniko IA, Grechukh TG. Some geologic-geochemical consequences of Dagestan earthquake of May 14, 1970. *Doklady Akademii nauk SSSR* 1972; **202**(3):576–579.
5. Osika DG. *Fluid Regime of Seismically Active Regions (Fluidniy Rejim Seismicheski-Aktivnikh Oblastey)*. Nauka Press (in Russian): Moscow, Russia, 1981.
6. Simkin EM, Lopukhov GP. Vibro-wave and vibro-seismic methods of oil reservoirs stimulation (a review). *Ser. Oil Industry (Neftianaya Promyshlennost)* 1989; **15**.
7. Beresnev IA, Johnson PA. Elastic-wave stimulation of oil production: a review of methods and results. *Geophysics* 1994; **59**(6):1000–1017.
8. Kouznetsov OL, Simkin EM, Chilingar GV, Katz SA. Improved oil recovery by application of vibro-energy to waterflooded sandstones. *Journal of Petroleum Science and Engineering* 1998; **19**(34):191 –200.
9. Westermark RV, Brett JF, Maloney DR. Enhanced oil recovery with downhole vibration stimulation. *SPE Production and Operations Symposium*, Society of Petroleum Engineers, SPE-67303-MS, Oklahoma City, Oklahoma, 2001.
10. Spanos T, Davidson B, Dusseault M, Shand D, Samaroo M. Pressure pulsing at the reservoir scale: a new IOR approach. *Journal of Canadian Petroleum Technology* 2003; **42**(02).
11. Zhu T, Xutao H, Vajjha P. Downhole harmonic vibration oil-displacement system: a new IOR approach. *SPE Western Region Meeting*, Society of Petroleum Engineers, SPE-94001, Irvine, CA, 2005.
12. Barabanov VL, Pavlov MV. Increasing oil production from depleted fields through seismic stimulation. *First break* 2009; **27**(3).
13. Elkhoury JE, Brodsky EE, Agnew DC. Seismic waves increase permeability. *Nature* 2006; **441**:1135–1138.
14. Chun H. Improved oil recovery by seismic vibration: a preliminary assessment of possible mechanisms. *SPE international Oil Conference and Exhibition*, Society of Petroleum Engineers, SPE-103870-MS, Cancun, Mexico, 2006.
15. Jeong C, Huh C, Kallivokas LF. On the feasibility of inducing oil mobilization in existing reservoirs via wellbore harmonic fluid action. *Journal of Petroleum Science and Engineering* 2011; **76**(34):116 –123.
16. Jeong C, Kallivokas LF, Huh C, Lake LW. Estimation of oil production rates in reservoirs exposed to focused vibrational energy. *SPE Improved Oil Recovery Symposium*, Society of Petroleum Engineers, SPE-169079-MS, Tulsa, Oklahoma, USA, 2014.
17. Manga M, Beresnev I, Brodsky EE, Elkhoury JE, Elsworth D, Ingebritsen SE, Mays DC, Wang CY. Changes in permeability caused by transient stresses: field observations, experiments, and mechanisms. *Reviews of Geophysics* 2012; **50**(2).
18. Candela T, Brodsky EE, Marone C, Elsworth D. Laboratory evidence for particle mobilization as a mechanism for permeability enhancement via dynamic stressing. *Earth and Planetary Science Letters* 2014; **392**(0):279 –291.
19. Roberts PM, Abdel-Fattah AI. Seismic stress stimulation mobilizes colloids trapped in a porous rock. *Earth and Planetary Science Letters* 2009; **284**(3):538–543.
20. Beresnev IA, Deng W. Viscosity effects in vibratory mobilization of residual oil. *Geophysics* 2010; **75**(4):N79–N85.
21. Beresnev I, Gaul W, Vigil RD. Direct pore-level observation of permeability increase in two-phase flow by shaking. *Geophysical Research Letters* 2011; **38**(20).
22. Deng W, Cardenas MB. Dynamics and dislodgment from pore constrictions of a trapped nonwetting droplet stimulated by seismic waves. *Water Resources Research* 2013; **49**(7):4206–4218.
23. Kurlenya MV, Serdyukov SV. Reaction of fluids of an oil-producing stratum to low-intensity vibro-seismic action. *Journal of Mining Science* 1999; **35**(2):113–119.
24. Kostrov SA, Wooden BO. Mechanisms, field suitability, and case studies for enhancement of oil recovery and production using in-situ seismic stimulation. *16th International Symposium on Nonlinear Acoustics*, Moscow, Russia, 2002.
25. Pride SR, Flekkøy EG, Aursjø O. Seismic stimulation for enhanced oil recovery. *Geophysics* 2008; **73**(5):O23–O35.
26. Parvulescu A, Clay CS. Reproducibility of signal transmission in the ocean. *The Radio and Electronic Engineer* 1965; **29**:223–228.
27. Fink M. Time reversal of ultrasonic fields – part I: basic principles. *IEEE Transactions on Ultrasonics, Ferroelectrics, and Frequency Control* 1992; **39**(5):555–566.
28. Anderson BE, Griffa M, Larmat C, Ulrich TJ, Johnson PA. Time reversal. *Acoustics Today* 2008; **4**(1):5–16.
29. Givoli D, Turkel E. Time reversal with partial information for wave refocusing and scatterer identification. *Computer Methods in Applied Mechanics and Engineering* 2012; **213216**:223–242.
30. Koo S, Karve PM, Kallivokas LF. A comparison of time-reversal and inverse-source methods for the optimal delivery of wave energy to subsurface targets. *Wave Motion* 2016; **67**:121–140.
31. Bamberger A, Chavent G, Lailly P. About the stability of the inverse problem in 1-D wave equations-application to the interpretation of seismic profiles. *Applied Mathematics and Optimization* 1979; **5**(1):1–47.
32. Tarantola A. Inversion of seismic reflection data in the acoustic approximation. *Geophysics* 1984; **49**(8):1259–1266.
33. Bunks C, Saleck F, Zaleski S, Chavent G. Multiscale seismic waveform inversion. *Geophysics* 1995; **60**(5):1457–1473.
34. Epanomeritakis I, Akçelik V, Ghattas O, Bielak J. A Newton-CG method for large-scale three-dimensional elastic full-waveform seismic inversion. *Inverse Problems* 2008; **24**(3):034015.
35. Kallivokas LF, Fathi A, Kucukcoban S, Stokoe(II) KH, Bielak J, Ghattas O. Site characterization using full waveform inversion. *Soil Dynamics and Earthquake Engineering* 2013; **47**(0):62 –82. SI: José Manuel Roësset.
36. Fathi A, Kallivokas LF, Poursartip B. Full-waveform inversion in three-dimensional PML-truncated elastic media. *Computer Methods in Applied Mechanics and Engineering* 2015; **296**:39 –72.

37. Fathi A, Poursartip B, Stokoe(II) K, Kallivokas LF. Three-dimensional P- and S-wave velocity profiling of geotechnical sites using full-waveform inversion driven by field data. *Soil Dynamics and Earthquake Engineering* 2016; **87**:63 –81.
38. Jeong C, Kallivokas LF, Huh C, Lake LW. Optimization of sources for focusing wave energy in targeted formations. *Journal of Geophysics and Engineering* 2010; **7**(3):242.
39. Jeong C, Kallivokas LF, Huh C, Lake LW. Maximization of oil mobility within a hydrocarbon reservoir for elastic wave-based enhanced oil recovery. *SPE Annual Technical Conference and Exhibition, SPE 147150*, Society of Petroleum Engineers, Denver, CO, USA, 2011.
40. Jeong C, Kallivokas LF, Kucukcoban S, Deng W, Fathi A. Maximization of wave motion within a hydrocarbon reservoir for wave-based enhanced oil recovery. *Journal of Petroleum Science and Engineering* 2015; **129**(0): 205–220.
41. Karve PM, Kucukcoban S, Kallivokas LF. On an inverse source problem for enhanced oil recovery by wave motion maximization in reservoirs. *Computational Geosciences* 2015; **19**(1):233–256.
42. Karve PM, Kallivokas LF. Wave energy focusing to subsurface poroelastic formations to promote oil mobilization. *Geophysical Journal International* 2015; **202**(1):119–141.
43. Fathi A, Poursartip B, Kallivokas LF. Time-domain hybrid formulations for wave simulations in three-dimensional PML-truncated heterogeneous media. *International Journal for Numerical Methods in Engineering* 2015; **101**(3):165–198.
44. Gunzburger MD. *Perspectives in Flow Control and Optimization*. SIAM: Philadelphia, PA, USA, 2003.
45. Petra N, Stadler G. Model variational inverse problems governed by partial differential equations. *Technical Report 11-5*, The Institute for Computational Engineering and Sciences, The University of Texas at Austin: Austin, TX, USA, 2011.
46. Sánchez-Sesma FJ, Weaver RL, Kawase H, Matsushima S, Luzón F, Campillo M. Energy partitions among elastic waves for dynamic surface loads in a semi-infinite solid. *Bulletin of the Seismological Society of America* 2011; **101**(4):1704–1709.
47. Karve PM, Kallivokas LF, Manuel L. A framework for assessing the uncertainty in wave energy delivery to targeted subsurface formations. *Journal of applied geophysics* 2016; **125**:26–36.